

1 **Characteristics of ozone and particles in the near-surface**
2 **atmosphere in urban area of the Yangtze River Delta, China**

3 **Huimin Chen¹, Bingliang Zhuang¹, Jane Liu^{1,2}, TijianWang¹, Shu Li¹, Min Xie¹, Mengmeng**
4 **Li¹, Pulong Chen¹, Ming Zhao¹**

5 **¹School of Atmospheric Sciences, CMA-NJU Joint Laboratory for Climate Prediction**
6 **Studies, Jiangsu Collaborative Innovation Center for Climate Change, Nanjing University,**
7 **Nanjing 210023, China**

8 **²Department of Geography and Planning, University of Toronto, Toronto, M5S 3G3, Canada**

9
10 **Abstract**

11 Aerosols and ozone have significant influences on air qualities, human health and climate changes.
12 To further understand the characteristics and interactions among different urban air pollutants in the
13 west Yangtze River Delta (YRD) region, continuous measurements of low layer atmospheric
14 particles and trace gases have been performed at an urban site in Nanjing from September 2016 to
15 February 2017 in this study. In urban area of west YRD, the mean PM₁₀ and O₃ concentrations are
16 86.3 μg/m³ and 37.7 ppb, respectively, with significant seasonal and diurnal variations. Particles,
17 which are dominated by fine aerosols, are relatively scattering. And most of their optical properties
18 have the similar variations to the aerosol concentrations. Results also show that west YRD could
19 still suffer severe air pollutions, although the seasonal mean aerosol concentrations have been
20 decreased in recent years. Even in cold seasons, O₃ could have about 40 days excess against to the
21 National Ambient Air Quality Standards during the sampling period. Most of polluted episodes are

22 caused by local and sub-regional emissions. A case study for a typical O₃ and PM_{2.5} episode in
23 December 2016 demonstrates that the episode was generally associated with regional transport and
24 stable weather system. Air pollutants were mostly transported from the western areas with high
25 emissions, as well as with an anticyclone and high-pressure system in this region. Correlation
26 analysis reveals that the interaction between O₃ and PMs are complex with a combination of
27 inhibition and promotion under different conditions. The inhibition effect might result from the
28 reduction of photolysis frequency near surface due to aerosols besides their positive correlations
29 with precursors, while the promotion effect is from the formation of secondary aerosols under high
30 concentrations of oxidants and solar radiation. However, the interaction between O₃ and BC shows
31 an inhibit effect due to its chemical stability. It is also indicated a VOC-sensitive regime for
32 photochemical production of O₃ in this region. This study further improves the insight in the
33 characteristics and interactions of main pollutants, and might have a certain contribution to improve
34 the simulation and prediction of aerosols and gases in urban area of YRD.

35

36 **1. Introduction**

37 Particles, including black carbon (BC), PM_{2.5}, and PM₁₀, and trace gases, such as carbon monoxide
38 (CO), ozone (O₃), nitric oxide and nitrogen dioxide (NO_x), and total reactive nitrogen (NO_y, which
39 includes NO_x, aerosol nitrates (NO₃⁻), nitric acid (HNO₃), N₂O₅, peroxyacetyl nitrate (PAN), and
40 various nitrogen-containing organic compounds.), are important components in the troposphere
41 because of their impacts on human health, biosphere and climate changes (e.g., Chameides et al.,
42 1999a, b; Jerrett et al., 2009; Allen et al., 2012). Through long-range particle cycles, particles could
43 interact with atmospheric trace gases from complex sources, especially ozone and its precursors,
44 disturbing the earth's radiation budget (Sassen, 2002), or providing reactive surfaces for

45 heterogeneous reactions (Kumar et al., 2014), which leads to a great but hard problem for regional
46 air quality (Zhang et al., 2008; van Donkelaar et al., 2010).

47

48 Over the decades, China is always one of the major source regions of particles, with BC and dust
49 emission accounting for up to 25% of the global anthropogenic sources (Streets et al., 2001; Tegen
50 and Schepanski, 2009). Relatively high levels of particle concentrations are mainly distributed in
51 Beijing-Tianjin-Hebei area (BTH), Yangtze River Delta (YRD), and Pearl River Delta (PRD) regions
52 (e.g., Zhang et al., 2008, 2012; Zhang et al., 2015), along with the rapid economic development.
53 These regions consistently have the highest emissions of anthropogenic precursors (e.g., Wang et
54 al., 2015; Wang et al., 2009b; Ding et al., 2013b; Zheng et al., 2010), which have led to severe
55 region-wide air pollution. Earlier studies on particles mostly focused on concentrations estimation,
56 the chemical characteristics, potential sources, as well as climate effects based on numerical
57 simulations (e.g., Wu et al., 2012; Song et al., 2014; Xiao et al., 2012; Yu et al., 2015; Kristjánsson,
58 2002; Liao and Seinfeld, 2005; Zhuang et al., 2010, 2013, 2013b, 2018). However, a better
59 understanding of spatial and temporal variations of particles can contribute to the adoption of
60 effective measures to reduce air pollution, and real-time monitoring data is essential to better obtain
61 the detailed variations (seasonal, monthly, and diurnal) on the city scale. In China, the research
62 based on PMs observations, especially in the polluted regions above, have gradually expanded since
63 2012 due to the establishment of China's PM_{2.5} air quality standards and gradual developments of
64 nationwide PMs observation. The research is mainly related to the temporal and spatial distribution
65 characteristics (e.g., Wang et al., 2015; Chen et al., 2016; Wu et al., 2012), and the effects of
66 meteorological variables on aerosols (e.g., Zhang et al., 2015; Yan et al., 2016; Huang et al., 2015).
67 In addition, many observations of BC have been made in the recent years, most of which
68 concentrated on the analysis of the concentration level and the temporal and spatial variations (e.g.,
69 Verma et al., 2010; Wang et al., 2011b; Zhang et al., 2012). Some also revealed the correlations of
70 carbonaceous aerosols (Pan et al., 2011; Zhuang et al., 2014b). Besides particles, because of the lack
71 of nationwide O₃ monitoring data in earlier years, O₃ and its precursors (NO_x, NO_y, CO and VOCs
72 etc.) pollution situations can only be discerned from limited campaign-type measurements in certain
73 developed regions, for instance, Beijing in BTH area (Shao et al., 2006; Lin et al., 2008; Meng et al.,

74 2009), Guangzhou in PRD region (Zhang et al., 1998; Wang et al., 2003) and Lin'an in YRD region
75 (Luo et al., 2000; Cheung and Wang 2001; Wang et al. 2001a, 2002, 2004; Guo et al. 2004b). Since
76 2005, the number of photochemical studies through observation data has increased in the PRD
77 region in the south (Xue et al., 2014a), the BTH area in the north (Han, 2011), and the YRD region
78 in the east (Shi et al., 2015). However, large gaps and uncertainties remain in the knowledge of
79 characteristics of regional particles and O₃ pollution and its mitigation strategies due to the
80 complexity of main sources, interaction between different aerosols, and changing meteorology filed.

81

82 The YRD is located in the eastern part of the Yangtze River Plain, adjacent to the most polluted
83 North China Plain, including large cities of Shanghai, southern Jiangsu and northern Zhejiang.
84 Taking up only 2 percent of the land area in China, this region produces over 20 percent of China's
85 Gross Domestic Product (GDP). Nanjing, as the capital of Jiangsu Province, lies in the middle to
86 west YRD. It covers an area over 6000 km², with more than 7.3 million residents
87 (<http://www.njt.gov.cn/>). Being the second largest commercial center after Shanghai in YRD, even
88 the East China, Nanjing is highly urbanized and industrialized, especially the urban area. In addition,
89 the complex monsoon and synoptic weather may play an important role in air pollution transport
90 and formation in Nanjing. Therefore, the urban atmosphere in Nanjing is also heavily polluted by
91 local emissions and long-distance transport of pollutants, which affects regional climate and air
92 quality (Huang et al., 2013; Yi et al., 2015). Thus, the issue of air pollution in Nanjing deserves
93 attentions. Previous studies using observation data in Nanjing often concentrated on characteristics
94 of one of the particles (Deng et al., 2011; Shen et al., 2014; Zhuang et al., 2014) or ozone and its
95 precursors (Tu et al., 2007; Wang et al., 2008; An et al., 2015), describing the temporal and spatial
96 distributions, and the influence of meteorological effects, but lay less emphasis on the inter-species
97 correlations and the combined effects of pollutants during severe pollution episodes. Ding et al.
98 (2013b) described the characteristics of O₃ and PM_{2.5} with near-surface observation data in rural
99 Nanjing, but the detailed characteristics in urban Nanjing is not clear enough so far.

100

101 To fill the knowledge gap, continuous online measurements of particles, trace gases, and other
102 relevant parameters were carried out at Gulou site in urban Nanjing about 80m above the ground,

103 an integrated measurement platform for the study of atmospheric environment and climate change.
104 In this study, 6-month measurement of particles, trace gases, and other related variables at this site
105 during September 2016~ February 2017 when air pollution occurred frequently is analyzed. Our
106 work gives a synthetic analysis about their characteristics. The emphasis of our objective is to
107 improve the insight in the characteristics, interactions of main pollutants, and the influence of
108 integrated meteorology variables based on the observation data at an urban site above ground, and
109 further investigate the possible underlying reasons and mechanisms. Firstly, an in-depth discussion
110 on particles variations is performed, not limited to the concentrations but taking optical properties
111 into consideration as well, to quantify the polluted level in detail. Secondly, a detailed description
112 of O₃ variations can also be found in our study, including the analysis of the main precursors as trace
113 gases (NO_x, NO_y and CO), to have a general and quantitative insight in O₃ pollution situations. Both
114 of the pollutants are analyzed considering the effects of meteorology variables including but not
115 limited to precipitation and temperature. Thirdly, analysis of inter-species correlations gives a
116 relatively thorough overview of the interactions among various species, and deduction of the
117 underlying chemical mechanisms based on the results of our study and previous studies is also
118 presented in our study. Moreover, backward trajectories analysis is conducted for improving the
119 knowledge of regional/sub-regional transport process in urban Nanjing. Finally, a case study for
120 high particles and O₃ episode is implementing to emphasize the integrated influence of
121 meteorological field on regional air pollution.

122

123 In the following, we describe the methodology in Section 2, which includes the measurement site
124 and instruments. Results and discussions are presented in Section 3, consisting of overall temporal
125 variation, correlation analysis, backward trajectory analysis, and case studies. A summary is given
126 in Section 4.

127

128 **2. Methodology**

129 **2.1 Brief Introduction to the Urban Atmospheric Observational Site**

130 The Urban Atmospheric Observational Site is a regional atmospheric urban site located on the Gulou
131 Campus of Nanjing University in the downtown area of Nanjing (32.05 °N, 118.78 °E), and run by
132 School of Atmospheric Sciences, Nanjing University. It is built on the roof of a 79.3m tall building,
133 without any industrial pollution sources within a 30 km radius around but several main roads with
134 evident traffic pollution, especially during rush hours. The sketch map of the site (not shown) and
135 the corresponding climatology have been described in Zhu et al (2012).

136

137 The particles, O₃, NO_x, NO_y (including most oxides of nitrogen mentioned above with the exception
138 of NH₃ and N₂O), CO, and wavelength-dependent aerosol optical parameters including aerosol
139 scattering (σ_{ts}), back-scattering (σ_{bs}), and absorption (σ_a) coefficients have been routinely
140 measured at the site during the time period from September 2016 to February 2017. The σ_a and
141 concentrations of BC were derived from the measurements using a seven-channel Aethalometer
142 (model AE-31, Magee Scientific, USA). The detailed calculation will be discussed below. The AE-
143 31 model measures light attenuation (ATN) at seven wavelengths, including 370, 470, 520, 590,
144 660, 880 and 950 nm. The sample air is taken through a stainless-steel tube into the instruments,
145 with a desired flow rate of 5.0 L min⁻¹ and a sampling interval of 5 min during the whole period.
146 The aerosol σ_{ts} and σ_{bs} were measured with a three-wavelength-integrating Nephelometer
147 (Aurora 3000, Australia). Aurora 3000 measures aerosol light scattering, including σ_{ts} and σ_{bs}
148 at 450, 525 and 635 nm, with a sampling interval of 1 min (Zhuang et al. 2017). The sample air was

149 taken through a 2m stainless-steel tube with a sampling interval of 1 min, top of which is 1.5m
150 above the roof. The inlet has a rain cap and an external as well as an internal heater to prevent
151 condensation. In cold seasons when RH in the tube was relatively low, maximum of which was
152 lower than 75% and 80% of which was lower than 50% during sunny hours, therefore the internal
153 heater was turned off. PM_{2.5} and PM₁₀ mass concentrations were measured using a mass analyzer
154 (Thermo Instruments, THOM 1405-DF), which has been used to measure the mass concentration
155 of PM_{2.5}, PM_{2.5-10}, and PM₁₀ simultaneously. The hourly and daily mean mass concentrations are
156 updated every 6 minutes, as well as the hourly base and reference mass concentrations. The sample
157 air is taken through a stainless-steel tube into the instruments. Trace gases (CO, NO_x, NO_y and O₃)
158 were measured every minute using online analyzers (Thermo Instruments, TEI 48i, 42i, 42iY, and
159 49i, respectively). Sample air was drawn from the 1.5m above the rooftop to the laboratory through
160 a manifold connected to O₃, NO_x and CO analyzers with PFA Teflon tubes, while a separate sample
161 line with a MoO converter was used for NO_y analyzer (Wang et al., 2002; Ding et al., 2013b) to
162 convert other reactive nitrogen species including PAN, NO₃⁻ and HNO₃. Thus the measured quantity
163 approximates total reactive nitrogen. Precision and instrument of all the measurements in this study
164 are listed in Table 1.

165

166 Since aerosols are quite hygroscopic in China (e.g., Eichler et al., 2008; Liu et al., 2011; Ding et al.,
167 2013b). All the instruments are installed in a laboratory with a constant temperature (24°C) and a
168 low RH located on the building roof. Routine calibrations and maintenances were carried out for all
169 these instruments during the sampling periods.

170

171 Monthly averaged meteorological parameters during the study period at the site are shown in Table
 172 2. The air temperature at the site ranged from 6.64°C in February to 24.88°C in September. Both
 173 higher relative humidity (RH) and more precipitation occurred in fall than winter, especially in
 174 October. Visibility (Vis) varied in different months. The peak of the ultraviolet radiation (UV)
 175 occurred in September, after which the radiation became weak till the end of January, and rose a
 176 little afterwards.

177

178 **2.2 Calculation of the aerosol optical properties**

179 The wavelength-dependent σ_a , which is associated with the intensities of the incoming light and
 180 remaining light after passing through a medium, can be calculated directly using the measured light
 181 attenuations (ATN) through a quartz filter matrix, a percentage to represent the filter attenuation, as
 182 well as BC mass concentrations (Petzold et al., 1997; Weingartner et al., 2003; Arnott et al., 2005;
 183 Schmid et al., 2006).

$$184 \quad \sigma_{a, ATN, t(\lambda)} = \frac{(ATN_t(\lambda) - ATN_{t-1}(\lambda))}{\Delta t} \times \frac{A}{V}, \quad (1)$$

185 where A (in m^2) is the area of the aerosol-laden filter spot, V is the volumetric sampling flow rate
 186 (in L min^{-1}) and Δt is the time interval (=5 min) between t and $t-1$. $\sigma_{a, ATN}$, known as σ_a
 187 without any correction, is larger than the actual aerosol absorption coefficient $\sigma_{a, \text{abs}}$ in general
 188 because of (1). multiple-scattering of light at the filter fibers (multiple-scattering effect), and (2) the
 189 instrumental response with increased particle loading on the filter (shadowing effect). The former
 190 results in the overestimation of the σ_a , while the later causes underestimation of the σ_a . Thus, the
 191 correction is needed and the calibration factors C and R (shown in Eq. 2) are introduced against the

192 scattering effect and shadowing effect, respectively:

$$193 \quad \sigma_{a, \text{abs}, t(\lambda)} = \frac{\sigma_{a, \text{ATN}, t(\lambda)}}{C \times R}, \quad (2)$$

$$194 \quad R_t(\lambda) = \left(\frac{1}{f} - 1\right) \times \frac{\ln(\text{ATN}_t(\lambda)) - \ln 10}{\ln 50 - \ln 10} + 1. \quad (3)$$

195

196 Previous investigation suggested that wavelength-dependent σ_a corrected by Schmid (Schmid et
197 al., 2006, SC2006 for short, hereinafter) might be the closest to the real ones in Nanjing (Collaud
198 Coen et al., 2010; Zhuang et al., 2015). Therefore, the SC2006 is adopted in this study. In this study,
199 the parameters in the correction procedure are derived from local optical properties (ω_0 and α_{ts}
200 were set to 0.922 and 1.51, respectively). The values of correction factors C and R are as follows:

201 $R=1$ when $\text{ATN} \leq 10$ and $f=1.2$, and C in Nanjing is 2.95, 3.37, 3.56, 3.79, 3.99, 4.51 and 4.64 at 370,
202 470, 520, 590, 660, 880 and 950 nm (Zhuang et al., 2015).

203

204 Measurement of Aurora 3000, a nephelometer with newly designed light sources based on light
205 emitting diodes, needs correction using Mie-theory for measurement artifacts. In this study,
206 correction was performed according to Müller et al. (2011). The raw total scattering coefficients
207 were corrected first by calculating first the Ångström exponents from the non-corrected scattering
208 coefficients and then following the formulas presented by Müller et al. (2011) where the tabulated
209 factors for no cutoff at the inlet were used. And based on corrected wavelength-dependent σ_a and
210 σ_{ts} , α_{ts} and α_a at 550 nm are estimated by the following:

$$211 \quad \alpha_{a, 470/660 \text{ nm}} = -\log(\sigma_{a, 470 \text{ nm}} / \sigma_{a, 660 \text{ nm}}) / \log(470/660), \quad (4)$$

$$212 \quad \alpha_{ts, 450/635 \text{ nm}} = -\log(\sigma_{ts, 450 \text{ nm}} / \sigma_{ts, 635 \text{ nm}}) / \log(450/635), \quad (5)$$

213

214 Meanwhile, aerosol asymmetry parameter (g), single-scattering albedo (ω_0) and extinction
215 coefficient (σ_e) are further estimated:

$$216 \quad \omega_0 = \frac{\sigma_{ts}}{\sigma_{ts} + \sigma_a}, \quad (6)$$

$$217 \quad \sigma_e = \sigma_{ts} + \sigma_a, \quad (7)$$

218

219 **2.3 HYSPLIT model**

220 In order to understand the general transport characteristics of air masses recorded at this site, we
221 conducted a 4 d (96 h) backward trajectory simulations during the cold seasons in 2016 using a
222 Lagrangian dispersion model Hybrid Single-Particle Lagrangian Integrated Trajectory (HYSPLIT)
223 (version 4.9) provided by the Air Resource Laboratory (ARL) of the USA National Oceanic and
224 Atmospheric Administration (NOAA) (Draxler and Hess, 1998). HYSPLIT - 4 Model is capable of
225 processing multiple gas input fields, multiple physical processes and different types of pollutant
226 emission sources and has been widely used in the study of transport and diffusion of various
227 pollutants in various regions (Mcgowan and Clark, 2008; Wang et al., 2011; Wang et al., 2015). It
228 is one of the most extensively used atmospheric transport and dispersion models for the study of air
229 parcel trajectories (Draxler and Rolph, 2013; Stein et al., 2016). In this study, backward trajectories
230 were calculated and clustered using a stand-alone version of the GDAS (Ground Data Acquisition
231 System) meteorological field (<ftp://arlftp.arlhq.noaa.gov/pub/archives/gdas1>). The GDAS data
232 contain 6-hourly basic meteorological fields on pressure surfaces, with the spatial resolution of 1.0 °,
233 corresponding to the 00, 06, 12, 18 UTC, respectively. In this study, the data are also converted to
234 hemispheric 144 by 73 polar stereographic grids, which is the same grid configuration as the dataset

235 applied in synoptic weather classification. For each synoptic weather pattern, the backward
236 trajectories were started at Gulou site in Nanjing (32°N, 118.8°E).

237 **3. Results and discussion**

238 **3.1 Characteristics of particulate matter in Nanjing**

239 The hourly-mean concentrations and optical properties of particles at Gulou site during the cold
240 seasons in 2016 are shown in Fig 1. Gaps in the time series are missing values. Observations show
241 that peaks and valleys of BC, PM_{2.5} and PM₁₀ occur simultaneously in general (Fig 1a), probably
242 because the three particles originate mostly from the same sources, i.e., fossil fuel burning and traffic
243 activities. It has also been addressed in previous work (e.g., Wang et al., 2008; Chow et al., 2011;
244 Schleicher et al., 2013; Zhuang et al., 2014b; Gong et al., 2015).

245

246 BC concentration ranged from 0.064 to 15.609 µg/m³. Seasonal mean of BC concentration was
247 2.126 µg/m³ in SON and 3.083 µg/m³ in DJF, with a standard deviation of 1.457 and 1.827 µg/m³,
248 respectively. It was low in September and October, usually below 6 µg/m³, but higher in other
249 months. Although BC concentration was relatively low, it was extremely high in particular periods, ,
250 such as in mid-November, early and late December, early January, and mid-to-late February,
251 suggesting occurrences of substantial BC pollution events. PM_{2.5} and PM₁₀ concentration ranged
252 from 0.8 to 256.4 µg/m³ and from 1.1 to 343.4 µg/m³, respectively. Seasonal mean of PM_{2.5}
253 concentration was 43.1 µg/m³ in SON and 73.2 µg/m³ in DJF, with a standard deviation of 25.4 and
254 40.0 µg/m³, respectively. PM₁₀ averaged 67.6 µg/m³ in SON and 105.0 µg/m³ in DJF, with a standard
255 deviation of 39.1 and 54.0 µg/m³, respectively. PM_{2.5} and PM₁₀ concentration were generally below

256 120 and 200 $\mu\text{g}/\text{m}^3$, respectively. Remarkable increases existed especially when BC concentration
257 was high. Additionally, the high concentrations of PMs in early October possibly resulted from the
258 increase in scattering aerosols, since absorption coefficient and BC, one of typical absorbing
259 aerosols, did not show such peak, while scatter coefficient experienced a sharp increase during that
260 period. It is found that both BC and PMs levels in Nanjing became lower compared to those in
261 earlier years, which is possibly due to the strengthening energy conservation and reduction of
262 pollution emissions from 2014. For instance, seasonal average in SON and DJF were reported 4339
263 and 4189 ng/m^3 in urban Nanjing during 2012 in Zhuang et al. (2014b), and Ding et al. (2013b)
264 stated a 1-year average about 75 $\mu\text{g}/\text{m}^3$ of $\text{PM}_{2.5}$ in rural area of Nanjing from August 2011 to July
265 2012, while Wang et al. (2014) suggested that annual average of $\text{PM}_{2.5}$ and PM_{10} were 75 and 135
266 $\mu\text{g}/\text{m}^3$ in Nanjing during 2013, respectively.

267

268 Monthly variations of particles in the cold seasons in 2016 were distinguished (Fig.2). The
269 concentrations increased from October to December and decreased a little afterwards but remained
270 relatively high in January and February. The lowest monthly concentrations of BC, $\text{PM}_{2.5}$, and PM_{10}
271 occurred in October, being 1.8, 39.2, and 59.8 $\mu\text{g}/\text{m}^3$, respectively, while the highest monthly
272 concentrations occurred in December, being 3.7, 85.0, and 123.1 $\mu\text{g}/\text{m}^3$, respectively, which were
273 about twice of those in October. Monthly variations of BC were different from those in previous
274 studies in YRD. For instance, Pan et al. (2011) pointed out an extremely high concentration in
275 October in Mt. Huang, which was attributed to combustion of biomasses as well as the dynamic
276 transport and stable planetary boundary layer (PBL) stratification in the transitional periods of the
277 winter monsoon (October). For PMs, monthly behavior was basically similar to what has been

278 reported in previous studies in YRD, increasing from September to December in general (Chen et
279 al., 2016), except the decrease in October. Generally, two key factors could impact particle
280 concentrations: meteorology and emissions. Heavy precipitation in October when average rainfall
281 was 3.1 mm, and the frequency of daily rainfall exceeding 50mm was over 30% (Table.2), had a
282 strong scavenging effect, which might directly lead to low levels of particles despite the influence
283 of biomass burning addressed in Pan et al. (2011). Anthropogenic particle emissions from fossil fuel
284 over China increased after summer and showed a sharp increase from November to January (Zhang
285 et al., 2009), and emission rates in southwest (Sichuan basin), central to north, and northeast China,
286 as well as YRD and PRD were higher in winter (Zhuang et al., 2018), especially in residential,
287 industry and power emissions (Li et al., 2017). And during the autumn harvest (September~
288 November), though not so much as that in summer, the crop burning emissions in still make
289 contribution to pollutants (Yang et al., 2008). Yin et al. (2016) discussed the spatial distribution of
290 crop residue burning from September to December in 2015, suggesting autumn crop residue burning
291 in surrounding regions like Shandong, Anhui and Henan Provinces, thus, particles in Nanjing might
292 also be subject to these large-scale burning of crop residues (Qian et al., 2014). According to Huang
293 et al. (2012) and Li et al. (2016), spatiotemporal distribution of agricultural fire occurrences in China
294 during 2003~ 2010 as well as 2012 has been presented associated with the spatial distribution of
295 CO emission from residue open burning. Both of them suggested the crop residue burning in autumn
296 is noteworthy and Jiangsu as well as the surrounding provinces are the regions with highest
297 emissions. Besides, sub-regional transport also plays an important role, for example, in winter, air
298 masses coming from North China Plain, which accounts for 31%, have high particles concentrations
299 (Sect 3.4).

300

301 Substantial diurnal cycles of the particles are also observed (Fig.3). Particles levels were high during
302 7:00~9:00 and 22:00~0:00 LT but low in afternoon (13:00~15:00 LT). High concentrations during
303 7~9 am might be caused by the vehicle emissions (as mentioned in Section 2, several main roads
304 with apparent traffic pollution surround the site). A higher vehicle volume showed during 17:00~
305 20:00 LT in Nanjing, while the high concentrations occurred during 22:00~ 0:00 LT. A lower
306 temperature and a more stable atmosphere stratification after sunset (17:00~18:00 LT) often lead to
307 frequent temperature inversion and low height of planetary boundary layer (Jiang et al., 2014),
308 which is not conducive to the diffusion of pollutants, and the concentrations of particles accumulate
309 and remain high from the evening to early morning. For low levels in afternoon, it is mainly induced
310 by well-developed boundary layer. Because the atmosphere become less stable with the increasing
311 temperature, and strong turbulent exchange as well as vertical diffusion are favorable to the
312 diffusion of pollutants, particles concentrations decrease to a minimum in the afternoon. Similar
313 phenomenon of PMs has been observed in previous studies in Nanjing (Chen et al., 2016; Ding et
314 al., 2013b), while a different pattern is discussed in Pan et al. (2011) in Mt. Huang, a rural site in
315 YRD, due to different emission sources (less vehicle emission) and meteorology effects (effect of
316 valley breezing). Fig. 3 also shows that the peak values of fine particle concentrations often occur
317 one or two hours later than those of BC concentrations, with high values at around 10 am and low
318 values at around 5 pm. According to Roberts and Friedlander (1976) and Khoder (2002),
319 atmospheric photochemical reactions are extremely active under conditions of strong radiation and
320 high temperature especially during daytime, thus, more secondary aerosol particles (like sulfate
321 particles) are likely to generate, and the concentrations of fine particles in the atmosphere will

322 increase.

323

324 **3.2 Characteristics of trace gases in Nanjing**

325 Fig.4 shows hourly-mean concentrations of trace gases at Gulou site during the cold seasons in 2016.

326 In general, as main precursors of O₃, NO_x, NO_y, and CO generally show different pattern with O₃,

327 such as when the precursors levels remained high from November to January, O₃ levels were

328 relatively low (Xie et al., 2016; Wang et al., 2017). Also, the precursors concentrations varied

329 greatly, especially in DJF (with several peaks), possibly because of the frequent shifting of air

330 masses from the clean interior continent and heavily polluted urban plumes in the heating period

331 (normally from November to March in Northern China) (Pan et al., 2011).

332

333 Concentrations of trace gases, including CO (176~ 2852 ppb), NO_x (2.7~ 80.0 ppb), NO_y (3.6~

334 158.4 ppb), and O₃ (0.2~ 235.7 ppb), varied a lot in the study period. Seasonal mean of O₃ was 42.3

335 ppb in SON and 33.1 ppb in DJF, with a standard deviation of 40.1 and 24.4 ppb, respectively. As

336 shown in Fig.4, O₃ concentration was extremely high during the entire September in 2016, with a

337 maximum over 200 ppb, and decreased sharply after mid-October, basically keeping a low level

338 below 100 ppb, until early February when it began to increase. Seasonal averages of NO_x and NO_y,

339 were 21.4 and 28.6ppb in SON, with a deviation of 20.5, and 40.1 ppb, respectively. In DJF, mean

340 concentrations of NO_x and NO_y were 27.6 and 37.0 ppb, with a deviation of 15.5 and 23.1 ppb. And

341 seasonal averages of CO were 753 ppb in SON, and 950 ppb in DJF, with a deviation of 353 and

342 388 ppb, respectively. The precursors concentrations were high from November to mid-January,

343 and low in September. Moreover, it is suggested that O₃ concentration is higher compared to the
344 results in previous studies based on the measurement at ground sites in Nanjing (Xie et al., 2016;
345 An et al., 2015; Ding et al., 2013b), implying a more pressing environmental issue of near-surface
346 O₃ problem in urban area.

347

348 Monthly variations of trace gases are shown in Fig.5. It is noticeable that the different patterns occur
349 in O₃ and its precursors. Observations show that O₃ concentration decreased after the lasting
350 extremely high level in September until November and increased a little afterwards. Highest
351 concentration of O₃ was found in September and lowest in November, being 74.8 and 23.4 ppb,
352 respectively. This pattern might be attributed to the solar radiation and emissions. For instance, in
353 September when solar radiation was strong (maximum UV over 55 W/m²), it would contribute
354 greatly to O₃ formation, and precursors were at relatively high levels (CO, NO_x, and NO_y were about
355 600, 15 and 20 ppb, respectively), though not as high as those in cold days. CO, NO_x and NO_y
356 peaked in December correspondingly at 1064, 31.8 and 41.7 ppb. The precursors reached the lowest
357 level in September, being 620, 14.5, and 20.8 ppb, respectively. In addition, the pattern of precursors
358 is analogous to those in previous studies (Xie et al., 2016; Ding et al., 2013b), but with a relatively
359 lower concentration, especially NO_x and NO_y, which might also result from the large-scale reduction
360 of pollution emissions.

361

362 Fig. 6 (a) shows the diurnal variations of the trace gases (O₃, NO_x, NO_y, and CO). The concentration
363 of O₃ is the lowest around 7:00 LT and rises rapidly until reaching the peak in the middle of the day
364 at 15:00 LT. It keeps decreasing sharply after the afternoon peak till sunset. During the nighttime,

365 the concentration of O₃ decreases slowly and remains low. With respect to NO_x and NO_y, peak
366 appears at around 9:00 LT, with another high value occurring at night (21:00~ 0:00 LT), both of
367 which coincide with the rush hours in the city, when large amounts of vehicle emissions are released.
368 The morning peak is slightly higher than the night one in general. Besides emissions, these diurnal
369 variation patterns of O₃ and NO_x (NO_y) mainly result from the photochemical processes and the
370 meteorological conditions. Simultaneous measurement of O₃ and UV shows that the O₃
371 concentration is highly correlated to UV (R=0.47). The ultraviolet radiation (UV) at Gulou started
372 to increase at about 7:00 LT (Fig.6 (b)), which could induce a series of photochemical reactions
373 including the formation of peroxy radicals (HO₂ and RO₂ etc.) and the photolysis of NO₂. From
374 8:00 to 15:00 LT, the increase in UV enhances the O₃ formation by promoting the production of
375 NO₂ and OH from NO and peroxy radicals. The diurnal range of O₃ concentration (the difference
376 between the maximum at 15:00 LT and the minimum at 7:00 LT) is relatively high (45.1 ppb),
377 suggesting the active chemical reactions as well. It is also noticeable that the O₃ peaks 2 hours after
378 the UV maximum, suggesting the time to take for the chemical reactions. The slightly reduction of
379 O₃ and NO_x in the early morning (3:00~7:00 LT) is likely due to NO_x titration. The development of
380 the planetary boundary layer (PBL) can also modulate pollutant concentrations. The concentration
381 of a pollutant is diluted when PBL rises during the daytime and enhanced in the low nocturnal PBL
382 that favors pollutant accumulation, after comparing Fig.6 (a) with the reported diurnal variation of
383 PBL height in Nanjing (Jiang et al., 2014; Xie et al., 2016). And that is also the reason for the
384 difference of peak time between the emission rate and NO_x (NO_y) concentration, which is similar
385 to particles to some degree. The abovementioned diurnal cycles in O₃ and NO_x (NO_y) concentration
386 follow the typical patterns at other sites in Nanjing (Tu et al., 2007; Ding et al., 2013b; Xie et al,

387 2016). The daily variation of CO concentration is found to be similar to that of BC, such as morning
388 peak during rush hours, afternoon dip at around 15:00 LT, and accumulation at night. A remarkable
389 correlation has been found in a number of previous studies (e.g., Jennings et al., 1996; Derwent et
390 al., 2001; Badarinath et al., 2007; Spackman et al., 2008; Pan et al., 2011; Zhuang et al., 2014b).
391 Besides, BC is mostly produced by the incomplete combustion of carbonaceous material, and so is
392 carbon monoxide (CO) (Pan et al., 2011), thus, both BC and CO might come from the same sources,
393 mostly from combustions of domestic bio-fuel, industry-coal, and vehicle-gasoline (Zhuang et al.,
394 2014b). The effect of meteorology, i.e., the development of PBL, influences the diurnal pattern as
395 mentioned in Section 3.1, especially the afternoon dip and night accumulation. Moreover, as one of
396 main precursors of O₃, increase in O₃ levels in the afternoon might also contribute to the lowest
397 concentration at 15:00 LT.

398

399 Table 5 further provides the statistics of O₃, PM_{2.5} and PM₁₀ mass concentrations with a comparison
400 to the National Ambient Air Quality Standards in China (NAAQS-CN) released in 2012 by the
401 China State Council and will be implemented nationwide in 2016 (MEP, 2012). According to
402 NAAQS-CN for PM_{2.5} and PM₁₀ (75 µg/m³ of PM_{2.5} and 150 µg/m³ of PM₁₀ for 24h average
403 concentration), there were 48 days of PM_{2.5} exceedances, accounting for about 30% during the study
404 period, and 14 days of PM₁₀ exceedances, lower than the PM_{2.5} exceedances. Days of PMs
405 exceedances mainly occurred during DJF. The days of exceedances decreased. Ding et al. (2013b)
406 reported 99 days of PM_{2.5} exceedances in total from September 2011 to February 2012, and Wang
407 et al. (2014) suggested that non-attainment rates in Nanjing from September 2013 to February 2014
408 were over 40% and 70% in SON and DJF, respectively. These results suggest that particles control

409 policies are well-implemented in Nanjing although particles remain a severe pollution problem in
410 the YRD region. According to NAAQS-CN for O₃ (160 µg/m³ for 8 h average and 200 µg/m³ for 1
411 h average), 37 days of exceedances occurred (Table 5), covering 20% of the period and mostly in
412 September and February when the air temperature was relatively high. In contrast to particulate
413 matter, days of O₃ exceedances increases greatly. Wang et al. (2014) reported a 11.4% contribution
414 of O₃ as the major pollutant on non-attainment days in cold seasons in 2013 in south-east China,
415 and Tu et al. (2007) reported frequency of days with O₃ exceedance for cold seasons in 2000~2002
416 in urban Nanjing was 6.3%. O₃ levels in the rural areas are generally higher than those in the city
417 centers (Zhang et al., 2008; Geng et al., 2008; Xie et al., 2016). Thus, high O₃ concentration and
418 severe air pollution at Gulou, an urban site, probably imply a severer O₃ pollution problem in the
419 entire YRD region. Moreover, note that this study only discusses the O₃ concentration in the cold
420 seasons when it is relatively low, and it might suggest a severer problem in warm seasons.

421

422 **3.3 Inter-species correlations**

423 Correlations between different species have been analyzed to help interpret the data and gain
424 insights into the underlying mechanisms/processes. Because precipitation could impact wet
425 scavenging processes for particles and other aerosols (Table 6), the data in rainy condition has been
426 eliminated.

427

428 The scatter plot of O₃ and NO_x measured at the site color-coded with air temperature is given in
429 Fig.7 (a). As discussed in previous studies (Xie et al., 2016; Ding et al., 2013b), measured O₃

430 presents an overall negative correlation with NO_x . The negative correlation mainly exists for data
431 of relatively low air temperature, suggesting a titration effect of freshly emitted NO_x with O_3 ,
432 especially at nighttime. However, the slope gets less rigid when air temperature rises, and tend to
433 be positive with a high temperature (over 25°C) and low level of NO_x (below 30 ppb). These results
434 possibly suggest a strong photochemical production of O_3 in this region under high temperature
435 with strong radiation like in September, leading to the seasonal cycle pattern of O_3 shown in Fig. 5
436 (a).

437

438 Fig.7 (b) provides a scatter plot of $\text{PM}_{2.5}$ and visibility (Vis) color-coded with relative humidity
439 (RH). For a better understanding of the relationship between the variables, we have performed a
440 linear fit of the visibility with the $\text{PM}_{2.5}$ concentration when $\text{RH} \leq 70\%$, $70\% < \text{RH} \leq 80\%$, and 80%
441 $< \text{RH} \leq 90\%$, to find out the relationship among these factors, and the fitting curves are $[\text{PM}_{2.5}] =$
442 $366.72[\text{Vis}]^{-0.745}$ ($R^2 = 0.7196$), $[\text{PM}_{2.5}] = 337.16[\text{Vis}]^{-0.855}$ ($R^2 = 0.8692$), and $[\text{PM}_{2.5}] = 248.6[\text{Vis}]^{-$
443 0.852 ($R^2 = 0.8279$), respectively. It is found that visibility decreases with the concentration of $\text{PM}_{2.5}$
444 in a power function with a negative exponent, and the inverse relationship between visibility and
445 aerosols concentrations as well as relative humidity has also been discussed in previous studies
446 based on the observations in YRD (e.g., Deng et al., 2011; Xiao et al., 2011; Jiang et al., 2018). The
447 correlation is stronger than that in Lin'an, a rural site not far from Nanjing (Jiang et al., 2018). The
448 concentrations of particles would increase the extinction coefficient, while the visibility (Vis) is
449 related to the coefficients through:

$$450 \quad \text{Vis} = \frac{3.91}{\sigma_e} \quad (8)$$

451 where Vis is the visibility and σ_e is the extinction coefficient (Larson et.al, 1989). As for the

452 effect of relative humidity (RH) on the visibility, according to Mie theory, with the increase of the
453 relative humidity, the radius of the wet particle also increases, and so the extinction coefficient,
454 which leads to the decrease in visibility.

455

456 According to the scatter plots of $PM_{2.5}$ - O_3 and BC - O_3 color-coded with air temperature (Fig.8),
457 $PM_{2.5}$ and BC are negatively correlated with O_3 in general. It is also noticeable that a negative
458 correlation between $PM_{2.5}$ and O_3 could be found for low air temperature samples while a positive
459 correlation exists for those under a high temperature. Similar results were also found at a rural site
460 in Nanjing (Ding et al., 2013b). Besides, BC is in a negative correlation with O_3 under low air
461 temperature, but tend less-correlated with O_3 when the temperature rises. $PM_{2.5}$ is well-correlated
462 with O_3 precursors, such as NO_x (Fig.10 (b)) and CO . Therefore, the anti-correlation in Fig.8 (a) for
463 cold air is likely due to the titration effect of high NO concentrations associated with high primary
464 $PM_{2.5}$ levels. Additionally, the increasing slope under high air temperature might be related to the
465 formation of secondary fine particles, especially the high conversion rate of SO_2 to sulfate under the
466 effect of the high concentration of oxidants (O_3) and solar radiation (Roberts and Friedlander, 1976;
467 Khoder, 2002). Previous studies of $PM_{2.5}$ chemical compositions in Shanghai (Wang et al., 2006)
468 and Nanjing (Ding et al., 2013b) suggested that sulfate was the most dominate ion in $PM_{2.5}$. Ding et
469 al. (2013b) also suggested formation of secondary organic aerosols with high O_3 concentration could
470 lead to the positive correlation because biogenic emission of VOCs is high under a condition of high
471 air temperature and solar radiation in summer. However, the study is performed during cold seasons
472 when air temperature is relatively lower and the biogenic emission of VOCs are likely lower, so the
473 positive correlation is less pronounced. As for BC , it also shows a good correlation with NO_x (Fig.10

474 (c)) and CO, which contributes to the inverse correlation for cold air. Since BC is insoluble in polar
475 and non-polar solvents and still remains stable when air or oxygen is heated to 350 ~ 400 °C, it's
476 hard to be generated or cleared through chemical reactions. And that is probably the reason why the
477 correlation between BC and O₃ is obscurer compared to the one between PM_{2.5} and O₃ when air
478 temperature rises. Moreover, as shown in Fig.9, O₃ is well correlated with UV (daily mean values
479 are used due to the remarkable diurnal variation), suggesting the significant role UV plays in O₃
480 production, while PM_{2.5} is generally negatively correlated with UV. Previous findings based on
481 various numerical models also suggest that particles can affect actinic flux of UV radiation, and
482 inhibit the photolysis reactions near surface in reducing the photolysis frequencies in the atmosphere,
483 like the frequency of O₃ → O(¹D) (e.g., Li et al., 2005; Deng et al., 2010; Li et al., 2011; Li et al.,
484 2018). In central Nanjing, as implied in Li et al. (2017), high concentrations of aerosols could result
485 in a 0.1–5.0 ppb (12.0%) reduction of near-surface ozone. Thus, they might result in the decrease
486 of O₃ concentration near the ground to some degree. However, the detailed mechanisms still need
487 to be further investigated by long-term measurement of aerosol chemical composition combined
488 with numerical models.

489

490 Scatter plots of CO–NO_x, PM_{2.5}–NO_x, and BC–NO_x, are given in Figs. 10 (a)~ (c), with data points
491 color-coded with the concentration of O₃. Fig.10 (b) and (c) show a good positive correlation
492 between PM_{2.5} and NO_x, as well as BC and NO_x as mentioned above, suggesting that the particles
493 at the site are mainly associated with similar sources like combustion and traffic activities (Wang et
494 al., 2006; Ding et al., 2013b; Zhuang et al., 2014b). It is found that high O₃ levels are generally
495 related to air masses of high CO/NO_x or particles/NO_x ratio. An increase in CO, as well as PM_{2.5}

496 and BC, always results in higher O₃ concentration for NO_x lower than 40 ppb, while NO_x reverses.
497 To be specific, when NO_x reduces for CO lower than 1500 ppb, O₃ has a sharp increase, and an
498 increase in the CO level would lead to an increase in the O₃ concentration, especially when NO_x
499 is lower than 40 ppb. The concentration of O₃ is sensitive to the level of its precursors, and the O₃
500 formation regime often includes NO_x-sensitive O₃ formation regime and VOCs-sensitive O₃
501 formation regime. If O₃ formation is under VOC-sensitive regime, a reduction in the NO_x
502 concentration will lead to an increase in the O₃ concentration, which is used to determine the O₃
503 photochemical production in the region is VOC-limited or NO_x-limited based on observation data
504 (Geng et al., 2008; Ding et al., 2013b). In our study, we have no VOCs measurement, thus CO is
505 chosen as the reference tracer, because mixing ratios of CO showed significant correlations with the
506 measured levels of most anthropogenic VOCs, which has been verified in many previous studies
507 (e.g., Baker et al., 2008; von Schneidemesser et al., 2010; Wang et al., 2014). In addition, as a
508 significant precursor of O₃, CO also plays a similar role as VOCs. HO₂ produced from the oxidation
509 reaction of CO with OH radicals could initiate photochemical reactions which result in the net
510 formation of O₃ (Novelli et al., 1998; Atkinson et al., 2000; Gao et al., 2005). Thus, the CO–O₃–
511 NO_x relationship may reflect the correlation of VOCs, NO_x, and O₃ in this region to some degree.
512 Therefore, we suggest that the region is VOC-sensitive. Geng et al. (2008) reported a VOC-sensitive
513 regime in urban Shanghai combining the measured and modeling results, and Ding et al. (2013b)
514 also reported a VOC-sensitive regime in rural area in Nanjing using the observation data. And the
515 PM_{2.5}-O₃-NO_x and BC-O₃-NO_x relationship show the similar pattern, possibly because they are
516 well-correlated with CO.

517

518 3.4 Backward Trajectory Analysis

519 The cluster means of the backward trajectory at 100 m from Gulou, Nanjing, in 2016 fall (Fig.11)
520 and winter (Fig. 13) suggest different air flows transported to Nanjing from long distances. In
521 general, the aerosol kinds and optical properties are characterized differently with different air
522 masses in the two seasons, which are further analyzed by their origins in SON and DJF (Figs.12 and
523 14). Figs. 12 and 14 show the main concentrations of particles and trace gases, the ratio of PM_{2.5} to
524 PM₁₀, as well as the values of the aerosol optical properties of different clusters during SON and
525 DJF, respectively. Because PM₁₀ varies similarly to PM_{2.5}, while NO_x varies analogously to NO_y,
526 we only present the variations of PM_{2.5} and NO_y with cluster here. Also, because σ_a , σ_{ts} and
527 σ_{bs} have good correlations with particle concentrations (Zhuang et al., 2014a) and g is greatly
528 affected by relative humidity, we discuss the variation of α_{ts} and ω_0 with cluster here.

529

530 In SON, the dominant air masses are from the East China Sea passing through urban agglomeration
531 regions (cluster 3), and less-developed regions (cluster 2) of the YRD, and from northern continent
532 away from Nanjing passing through oceans and urban agglomeration regions (cluster 4). It is found
533 that although air masses in cluster 3, cluster 4 and cluster 2 all pass through the oceans and have the
534 same level of RH, differences still exist among the clusters. The air masses have to cross the urban
535 agglomeration (from Shanghai to Nanjing) of YRD when they arrive in Nanjing in cluster 3 but pass
536 less-developed regions (north Jiangsu Province) in cluster 4 and cluster 2. In YRD, emissions of
537 aerosols and trace gases are much stronger in urban agglomeration regions (Zhang et al., 2009;
538 Zhuang et al., 2013). It is also noticeable that concentrations of aerosols in cluster 4 are mostly
539 lower, which may result from its avoidance from BTH regions, also a megacities and urban

540 agglomeration. In addition, air masses from the west of cluster 1 contain the highest concentrations
541 of PMs and precursors., Air masses pass central China with high emissions of particles and trace
542 gases according to MERRA data (<https://gmao.gsfc.nasa.gov/reanalysis/MERRA>) and Zhuang et
543 al. (2015). Also, high concentrations of these aerosols are also reflected in a high aerosol optical
544 depth (AOD) according to the MISR data (<https://giovanni.gsfc.nasa.gov/giovanni>). The ratio of
545 PM_{2.5} to PM₁₀ represents the number of particles deriving from secondary pollution progress
546 compared to those from primary pollution progress to some extent. In SON, ratios of clusters 1~3
547 are relatively close (all over 60%) with a maximum of cluster 3, which means particles generating
548 from secondary pollution progress in the 3 clusters have a similar rate. O₃ concentrations among the
549 4 clusters are different. Despite negative correlations of O₃ with its precursors and particles, the
550 concentration of O₃ in cluster 3 is higher than that in cluster 4, possibly because radiation in cluster
551 3 is stronger. The size of the aerosols in cluster 1 are finest (α_{ts} is the largest in Fig. 12g), because
552 the other 3 clusters all pass through oceans before arriving Nanjing with higher relative humidity.
553 Therefore, it is likely to enhance particles hygroscopicity. ω_0 is also the largest in cluster 1, and it
554 suggests that aerosols in cluster 1 are the most scattering, corresponding with the highest
555 concentration of PM_{2.5}.

556

557 In DJF, air masses come from the local region (cluster 2), north-west areas (cluster 1), and northern
558 regions far from Nanjing (cluster 4). Air masses from cluster 1 and cluster 2 both account for over
559 30% of the total aerosol characteristics and are more polluted with relatively high levels of particles,
560 CO, and NO_x. Air masses in cluster 1 come from Shandong Province while those in cluster 2 come
561 from local areas. Particles and trace gases concentrations of cluster 2 are higher than those of cluster

562 1 to some extent, implying the severer air pollution problem in YRD region. The concentration of
563 O₃, similar to that in SON, is affected by radiation besides precursors levels. Thus, O₃ concentration
564 in cluster 2 is a little higher than that in cluster 1. The ratios of PM_{2.5} to PM₁₀ of cluster 1 and cluster
565 2 are approximately equal, over 70%. The size of aerosols in cluster 1 and 2 are coarser, however,
566 probably due to the higher RH (over 65%). Aerosols in cluster 1 are more scattering compared to
567 those in cluster 2. The trajectories of cluster 3 and cluster 4 are analogous to those in SON,
568 respectively, but more polluted, probably due to more emissions in DJF especially in north China
569 and weaker flow from ocean in DJF.

570

571 **3.5 Case Study**

572 For further understanding of the causes for high pollutants episodes, especially high particles and
573 O₃ episodes, detailed analysis of a typical episode from 2016 December 3-6 is presented in this
574 section.

575

576 Fig.15 (a) and (b) show that high O₃ concentration (over 80 ppb) occurred on December 4 with
577 broad O₃ peaks (over 60 ppb) in the following days, while the average O₃ during the cold seasons
578 was 37.7 ppb. Though there is lack of PMs concentrations because of the instrument breakdown,
579 high concentrations of PMs might possibly occur referring to the relatively high σ_e (over 500
580 Mm⁻¹) and BC concentration (over 6 $\mu\text{g}/\text{m}^3$) on December 4th. Both PMs reach a maximum on
581 December 5th (PM_{2.5} over 200 $\mu\text{g}/\text{m}^3$ and PM₁₀ over 300 $\mu\text{g}/\text{m}^3$), over 3 times of the averages.
582 Besides, NO_x, NO_y, have reached high levels since December 4th (NO_x over 70 ppb and NO_y over

583 100 ppb). It is also noticeable that ω_0 has a relatively sharp decrease from December 4, especially
584 on December 5 when particle concentrations were extremely high, probably suggesting that the ratio
585 of PM₁₀ became higher. Meanwhile, a relatively sharp increase occurred in α_{ss} , without any
586 obvious variation in α_a , though, implying that scattering aerosols could take the leading role
587 during this episode. It is also found that this case occurred under calm conditions before the passage
588 of a cold front, which was at the front of a continental high-pressure system originating from
589 Mongolia and sweeping over Nanjing (Fig.15 (c)), and the decrease in temperature with high-
590 pressure system dominating eastern China were also detected on December 6. Backward trajectory
591 analysis for the past 96 hours (Fig.15 (d)) were conducted from December 5 at 8 pm, including the
592 maximum of O₃ on December 4 and PMs on December 5. It is suggested that predominant wind
593 was just in time from the NW directions. Therefore, air masses with high particles and O₃
594 concentrations would be transported to Nanjing. It was also clearly detected in Nanjing during these
595 days, such as the relatively high O₃ during nighttime on December 5 and 6. The highest O₃ on
596 December 4 together with high particles and primary pollutants NO_x and NO_y suggests a strong in
597 situ photochemical production in mixed regional plumes under the influence of high-pressure
598 system. Previous studies (Luo et al., 2000; Wang et al., 2006; Ding et al., 2013b) reported that the
599 anticyclonic conditions, e.g., sunny weather and low wind velocities, are favorable for pollution
600 accumulation and O₃ production. Results in this case clearly demonstrate sub-regional transport of
601 primary and secondary air pollutants within the YRD region under such weather system.

602 **4. Conclusion**

603 In this study, particles (BC and PMs) and trace gases (O₃ and related precursors) in polluted seasons,

604 are investigated based on continuous measurements of concentrations and optical properties in the
605 urban area of Nanjing. The characteristics and underlying reasons are comprehensively discussed
606 from perspectives of temporal variations, inter-species correlations, trajectories analysis, and case
607 studies associated with weather data and Lagrangian dispersion modeling.

608

609 Measurements show that average concentrations of PM_{10} was $86.3 \mu\text{g}/\text{m}^3$, with BC and $PM_{2.5}$
610 accounting for 3% and 67%, respectively. 48 and 14 days of $PM_{2.5}$ and PM_{10} exceeded NAAQS-CN,
611 respectively. The results suggested that both BC and PMs levels in Nanjing have decreased because
612 of energy conservation since 2014. The average concentration of O_3 was 37.7 ppb with 40 days of
613 exceedance. Precursor concentrations, including CO, NO_x and NO_y , averaged 753, 28.4, and 28.6
614 ppb, respectively. Contrast to particles, O_3 concentration has increased in urban Nanjing, implying
615 a severer pollution in rural area and entire YRD region. All the aerosols have substantially monthly
616 and diurnal variations. Both particles and precursors reached maximum values in December and
617 minimum values in October due to higher emission and less precipitation. O_3 showed a peak in
618 September because of stronger radiation. Diurnal variations of BC and PMs were similar with peaks
619 around 7:00~9:00 and 22:00~0:00 LT. Both of the peaks were influenced by traffic emissions in
620 rush hours and accumulation of air pollution especially at night-time. The peaks of PMs often
621 occurred 1~ 2 h later than those of BC, possibly due to the production of secondary particles.
622 Precursors and particles varied similarly in time, and the diurnal variation of O_3 was analogous to
623 that of radiation with peak around 15:00 LT.

624

625 $PM_{2.5}$ has a quasi-power-law distribution with Vis under RH of different ranges. The correlation is

626 stronger than that in a rural region in YRD, implying greater effects of air pollution on visibility in
627 urban Nanjing. O₃ shows an anti-correlation with NO_x generally, but it tends to be positive with a
628 relatively high temperature and low level of NO_x. PM_{2.5} and BC are overall negatively correlated
629 with O₃. A positive correlation between PM_{2.5} and O₃ exists under high temperatures, while it is not
630 found in BC-O₃ correlation. The negative correlation is related to the titration effect of high NO
631 concentration, which is highly correlated with particles due to similar emission sources. And the
632 negative correlation between PM_{2.5} and UV suggests particles could decrease actinic flux of
633 radiation, and thus inhibit the photolysis reactions near surface to degrees. The positive correlation
634 implies the formation of secondary aerosols under the effects of the high concentrations of oxidants
635 and solar radiation. BC is hard to be generated through chemical reactions, which might explain
636 why the correlation between BC and O₃ is obscurer when temperature rises. An increase in CO, as
637 well as PM_{2.5} and BC, always results in higher O₃ concentration, while NO_x reverses, which
638 indicates a VOC-sensitive regime for photochemical production of O₃ in urban Nanjing.

639

640 Backward trajectories indicate that Nanjing could be affected by local air flow (35% in DJF) and
641 long-distance air flows mostly from western (11% in SON), northwestern (31% in DJF), northern
642 (up to 50 % in SON and DJF), eastern (40% in SON and 17% in DJF). Considerable air pollution
643 in the urban area of Nanjing is due to local and sub-regional emissions. Basically, air masses from
644 the oceans and remote or less-developed areas are relatively clean with low aerosols concentrations.
645 α_{rs} at the site is usually low when the relative humidity of air masses is high, possibly suggesting
646 the increased hygroscopicity and more secondary aerosols production under higher RH.

647

648 A case study for a typical high O₃ and PM_{2.5} episode in December 2016 illustrates the important
649 influences of sub-regional transport of pollutants from strong source regions and local synoptic
650 weather on the episode. Stable conditions such as an anticyclonic system make it easy for pollutants
651 to accumulate in urban Nanjing. Results from this case reveal the mechanisms of sub-regional
652 transport of primary and secondary air pollutants within the YRD region.

653

654 Overall, this work highlights the interactions and mechanisms of various aerosols and metrological
655 fields besides the important environmental impact from human activities and meteorological
656 conditions in the urban area in YRD region. Considering both results in this study and previous
657 work, it is suggested that collaborative control measures among different administrative regions are
658 urgently needed including but not limited to energy conservation and reduction of pollution
659 emissions to improve air quality in the western part of YRD region.

660

661 *Data availability.* The GDP data is from <http://www.njtc.gov.cn/>. Satellite CO data are available at:
662 <https://gmao.gsfc.nasa.gov/reanalysis/MERRA>. The aerosols AOD data are available at:
663 <https://giovanni.gsfc.nasa.gov/giovanni>. The Lagrangian dispersion model Hybrid Single-Particle
664 Lagrangian Integrated Trajectory (HYSPLIT) was supplied by NOAA:
665 http://ready.arl.noaa.gov/HYSPLIT_traj.php. The meteorological data for HYSPLIT are accessible
666 from <ftp://arlftp.arlhq.noaa.gov/pub/archives/gdas1>.

667

668 *Competing interests.* The authors declare that they have no conflict of interest.

669

670 *Author Contributions.* Huimin Chen, Bingliang Zhuang and Tijian Wang designed research; Huimin
671 Chen, Bingliang Zhuang, Jane Liu, and Shu Li performed research; Huimin Chen, Bingliang Zhuang,
672 Min Xie, Mengmeng Li, Pulong Chen and Ming Zhao analyzed data; and Huimin Chen, Bingliang
673 Zhuang, and Jane Liu wrote the paper.

674

675 *Acknowledgements.* This work was supported by the National Program of China
676 (2017YFC0209803, 2014CB441203, 2016YFC0203303), the National Natural Science Foundation
677 of China (41675143, 91544230, 41621005). The authors would like to thank all members in the
678 AERC of Nanjing University for maintaining instruments.

679

680

681 **References**

682 Allen, R. J., Sherwood, S. C., Norris, J. R., and Zender, C.S.: Recent Northern Hemisphere tropical
683 expansion primarily driven by black carbon and tropospheric ozone, *Nature*, 485,
684 doi:10.1038/nature11097, 350–353, 2012.

685 Anderson, T. L. and Ogren, J. A.: Determining aerosol radiative properties using the TSI 3563
686 integrating nephelometer, *Aerosol Sci. Tech.*, 29, 57–69, 1998.

687 An, J., Zou, J., Wang, J., Lin, X., Zhu, B., 2015. Differences in ozone photochemical characteristics
688 between the megacity Nanjing and its suburban surroundings, Yangtze River Delta, China.
689 *Environ. Sci. Pollut. Res.* 22, 19607–19617.

690 Arnott, W. P., Hamasha, K., Moosmuller, H., Sheridan, P. J., and Ogren, J. A.: Towards aerosol light-
691 absorption measurements with a 7-wavelength aethalometer: evaluation with a photoacoustic

692 instrument and 3-wavelength nephelometer, *Aerosol Sci. Technol.*, 39, 17–29,
693 doi:10.1080/027868290901972, 2005.

694 Atkinson, R.: Atmospheric chemistry of VOCs and NO_x, *Atmos. Environ.*, 34, 2063–2101,
695 doi:10.1016/S1352-2310(99)00460-4, 2000.

696 Badarinath, K. V. S., Kharol, S. K., Chand, T. R. K., Parvathi, Y. G., Anasuya, T., and Jyothsna, A.
697 N.: Variations in black carbon aerosol, carbon monoxide and ozone over an urban area of
698 Hyderabad, India, during the forest fire season, *Atmos. Res.*, 85(1), 18–26, 2007.

699 Baker, A. K., Beyersdorf, A. J., Doezema, L. A., Katzenstein, A., Meinardi, S., Simpson, I. J., Blake,
700 D. R., Rowland, F. S.: Measurements of nonmethane hydrocarbons in 28 United States cities,
701 *Atmos. Environ.*, 2008, 42(1): 170–182.

702 Chameides, W. L., Li, X., Tang, X., Zhou, X., Luo, C., Kiang, C. S., John, J. St., Saylor, R. D., Liu,
703 S. C., Lam, K. S., Wang, T., and Giorgi, F.: Is ozone pollution affecting crop yields in China,
704 *Geophys. Res. Lett.*, 26, 867–870, 1999b.

705 Chameides, W. L., Yu, H., Liu, S. C., Bergin, M., Zhou, X., Mearns, L., Wang, G., Kiang, C. S.,
706 Saylor, R. D., Luo, C., Huang, Y., Steiner, A., and Giorgi, F.: Case study of the effects of
707 atmospheric aerosols and regional haze on agriculture: An opportunity to enhance crop yields in
708 China through emission controls?, *PNAS*, 96, 13626–13633, 1999a.

709 Chen, T.; He, J.; Lu, X.W.; She, J.F.; Guan, Z.Q. Spatial and Temporal Variations of PM_{2.5} and Its
710 Relation to Meteorological Factors in the Urban Area of Nanjing, China. *Int. J. Environ. Res.*
711 *Public Health* 2016, 13, 921.

712 Cheung, V.T.F., Wang, T., 2001. Observational study of ozone pollution at a rural site in the Yangtze
713 Delta of China. *Atmos. Environ.* 35, 4947–4958.

714 Chow, J. C., Watson, J. G., Lowenthal, D. H., Chen, L.-W. A., Motallebi, N.: PM_{2.5} source profiles

715 for black and organic carbon emission inventories. *Atmospheric Environment*, 2011, 45(31):
716 5407-5414.

717 Collaud Coen, M., Weingartner, E., Apituley, A., Ceburnis, D., Fierz-Schmidhauser, R., Flentje, H.,
718 Henzing, J. S., Jennings, S. G., Moerman, M., Petzold, A., Schmid, O., and Baltensperger, U.:
719 Minimizing light absorption measurement artifacts of the Aethalometer: evaluation of five
720 correction algorithms, *Atmos. Meas. Tech.*, 3, 457–474, doi:10.5194/amt-3-457-2010, 2010.

721 Deng, J. J., Wang, T.J., Liu, L., Jiang, F.: Modeling heterogeneous chemical processes on aerosol
722 surface. *Particuology* 8 (4), 308-318, 2010.

723 Deng, J., Wang, T., Jiang, Z., Xie, M., Zhang, R., Huang, X., Zhu, J., 2011. Characterization of
724 visibility and its affecting factors over Nanjing, China. *Atmospheric Research* 101, 681-691.

725 Derwent, R. G., Ryall, D. B., Jennings, S. G., Spain, T. G., and Simmonds, P. G.: Black carbon
726 aerosol and carbon monoxide in European regionally polluted air masses at Mace Head, Ireland
727 during 1995–1998, *Atmos. Environ.*, 35(36), 6371–6378, 2001.

728 Ding, A. J., Fu, C. B., Yang, X. Q., Sun, J. N., Zheng, L. F., Xie, Y. N., Herrmann, E., Nie, W., Petaja,
729 T., Kerminen, V. -M., and Kulmala, M.: Ozone and fine particle in the western Yangtze River Delta:
730 an overview of 1 yr data at the SORPEs station, *Atmos. Chem. Phys.*, 13, 5813–5830, 2013b.

731 Draxler, R. R. and Hess, G. D.: An overview of the HYSPLIT 4 modeling system for trajectories
732 dispersion and deposition, *Aust. Meteor. Mag.*, 47, 295–308, 1998.

733 Draxler, R.R. and Rolph, G.D. (2013) HYSPLIT (HYbrid Single-Particle Lagrangian Integrated
734 Trajectory) Model Access Via NOAA ARL READY Website, NOAA Air Resources Laboratory,
735 Silver Spring, MD [online].

736 Eichler, H., Cheng, Y. F., Birmili, W., Nowak, A., Wiedensohler, A., Brüggemann, E., Gnauk, T.,
737 Herrmann, H., Althausen, D., Ansmann, A., Engelmann, R., Tesche, M., Wendisch, M., Zhang, Y.

738 H., Hu, M., Liu, S., and Zeng, L. M.: Hygroscopic properties and extinction of aerosol particles at
739 ambient relative humidity in South-Eastern China, *Atmos. Environ.*, 42, 25, 6321–6334.
740 doi:10.1016/j.atmosenv.2008.05.007, 2008.

741 Gao, J., Wang, T., Ding, A., Liu, C.: Observational study of ozone and carbon monoxide at the
742 summit of mount Tai (1534 m a.s.l.) in central-eastern China. *Atmos. Environ.*, 2005, 39(26),
743 4779–4791.

744 Geng, F. H., Tie, X. X., Xu, J. M., Zhou, G. Q., Peng, L., Gao, W., Tang, X., Zhao, C. S.:
745 Characterizations of ozone, NO_x, and VOCs measured in Shanghai, China. *Atmos. Environ.* 42,
746 6873–6883, 2008.

747 Gong, W., Zhang, T.H., Zhu, Z.M., Ma, Y.Y, Ma, X., Wang, W.: Characteristics of PM_{1.0}, PM_{2.5}
748 and PM₁₀ and their relation to black carbon in Wuhan, central China. *Atmosphere*, 2015, 6(9):
749 1377-1387.

750 Guo, H., Wang, T., Simpson, I., Blake, D., Yu, X., Kwok, Y., et al., 2004b. Source contributions to
751 ambient VOCs and CO at a rural site in eastern China. *Atmos. Environ.* 38, 4551–4560.

752 Han, S., 2011. Analysis of the relationship between O₃, NO and NO₂ in Tianjin, China. *Aerosol Air*
753 *Qual. Res.*

754 Huang, F., Li, X., Wang, C., Xu, Q., Wang, W., Luo, Y., Tao, L., Gao, Q., Guo, J., Chen, S.: PM_{2.5}
755 spatiotemporal variations and the relationship with meteorological factors during 2013–2014 in
756 Beijing, China. *PLoS ONE* 2015, 10, e0141642.

757 Huang, X., Li, M., Li, J., Song, Y.: A high-resolution emission inventory of crop burning in fields
758 in China based on MODIS Thermal Anomalies/Fire products. *Atmospheric Environment*, 2012,
759 50:9-15.

760 Huang, X. X., Wang, T. J., Jiang, F., Liao, J. B., Cai, Y. F., Yin, C. Q., Zhu, J. L., Han, Y., 2013.
761 Studies on a severe dust storm in East Asia and its impact on the air quality of Nanjing, China.
762 *Aerosol Air Qual. Res.* 13, 179e193.

763 Jennings, S. G., Spain, T. G., Doddridge, B. G., Maring, H., Kelly, B. P., and Hansen, A. D. A.:
764 Concurrent measurements of black carbon aerosol and carbon monoxide at Mace Head, *J. Geophys.*

765 Res. Atmos., 101(D14), 19447–19454, 1996.

766 Jerrett, M., Finkelstein, M. M., Brook, J. R., Arain, M. A., Kanaroglou, P., Stieb, D. M., Gilbert, N.
767 L., Verma, D., Finkelstein, N., Chapman, K. R., and Sears, M. R.: A Cohort Study of Traffic-
768 Related Air Pollution and Mortality in Toronto, Ontario, Canada. *Environmental Health*
769 *Perspectives*, 2009, 117(5):772-777.

770 Jiang, J., Zheng, Y. F., Liu, J. J., and Fan, J. J.: Observational research on planetary boundary layer
771 by lidar over Nanjing city. *Environ. Sci. Technol.* 37, 22–27 (in Chinese), 2014.

772 Jiang, L., Zhang, Z. F., Zhu, B., Shen, Y., Wang, H. L., Shi, S. S., Sha, D. D.: Comparison of
773 parameterizations for the atmospheric extinction coefficient in Lin'an, China. *The Science of the*
774 *total environment.*, 2018, 621. 507-515. 10.1016/j.scitotenv.2017.11.182.

775 Khoder, M. I.: Atmospheric conversion of sulfur dioxide to particulate sulfate and nitrogen dioxide
776 to particulate nitrate and gaseous nitric acid in an urban area, *Chemosphere*, 49, 675–684, 2002.

777 Kristjánsson, J.E., 2002. Studies of the aerosol indirect effect from sulfate and black carbon aerosols.
778 *Journal of Geophysical Research* 107 (D15), 4246.

779 Kumar, R., Barth, M.C., Madronich, S., Naja, M., Carmichael, G.R., Pfister, G.G., Knote, C.,
780 Brasseur, G.P., Ojha, N., Sarangi, T., 2014. Effects of dust aerosols on tropospheric chemistry
781 during a typical pre-monsoon season dust storm in northern India. *Atmos. Chem. Phys.* 14, 6813-
782 6834.

783 Larson, S.M., and Cass, G.R.: Characteristics of summer midday low-visibility events in the Los
784 Angeles area. *Environmental Science & Technology.* 23-281, 1989.

785 Liao, H., Seinfeld, J.H., 2005. Global impacts of gas-phase chemistry aerosol interactions on direct
786 radiative forcing by anthropogenic aerosols and ozone. *Journal of Geophysical Research* 110,
787 D18208.

788 Li, G. H., Zhang, R. Y., Fan, J. W.: Impacts of black carbon aerosol on photolysis and ozone. *Journal*

789 of Geophysical Research., 2005, 110(D23206).

790 Li, J., Bo, Y., Xie, S.: Estimating emissions from crop residue open burning in China based on
791 statistics and MODIS fire products. *Journal of Environmental Sciences*, 2016, 44:158-167.

792 Li, J., Wang, Z., Wang, X., Yamaji, K., Takigawa, M., Kanaya, Y., Pochanart, P., Liu, Y., Irie, H.,
793 Hu, B., Tanimoto, H., and Akimoto, H.: Impacts of aerosols on summertime tropospheric
794 photolysis frequencies and photochemistry over Central Eastern China, *Atmos. Environ.*, 45,
795 1817–1829, doi:10.1016/j.atmosenv.2011.01.016, 2011.

796 Li, M., Wang, T., Xie, M., Li, S., Zhuang, B., Chen, P.: Agricultural fire impacts on ozone
797 photochemistry over the Yangtze River Delta region, East China. *Journal of Geophysical*
798 *Research: Atmospheres*, 2018.

799 Li, M., Wang, T., Xie, M., Li, S., Zhuang, B., Chen, P.: Impacts of aerosol-radiation feedback on
800 local air quality during a severe haze episode in Nanjing megacity, eastern China, *Tellus B:*
801 *Chemical and Physical Meteorology*, 2017, 69(1):1339548.

802 Li, M., Zhang, Q., Kurokawa, J., Woo, J.-H., He, K. B., Lu, Z. F., Ohara, T., Song, Y., Streets, D.
803 G., Carmichael, G. R., Cheng, Y. F., Hong, C. P., Huo, H., Jiang, X. J., Kang, S., Liu, F., Su, H.,
804 Zheng, B.: MIX: a mosaic Asian anthropogenic emission inventory under the international
805 collaboration framework of the MICS-Asia and HTAP, *Atmos. Chem. Phys.*, 2017, 17, 935–963.

806 Lin, W., Xu, X., Zhang, X., Tang, J., 2008. Contributions of pollutants from North China Plain to
807 surface ozone at the Shangdianzi GAW Station. *Atmos. Chem. Phys.* 8, 5889–5898.

808 Liu, P. F., Zhao, C. S., Gobel, T., Hallbauer, E., Nowak, A., Ran, L., Xu, W. Y., et al.: Hygroscopic
809 properties of aerosol particles at high relative humidity and their diurnal variations in the North
810 China Plain, *Atmos. Chem. Phys.*, 3479–3494, doi:10.5194/acp-11-3479-2011, 2011.

811 Luo, C., St. John, J. C., Zhou, X. J., Lam, K. S., Wang, T., and Chameides, W. L.: A nonurban ozone
812 air pollution episode over eastern China: Observation and model simulation, *J. Geophys. Res.*, 105,
813 1889–1908, 2000.

814 McGowan, H. and Clark, A.: Identification of dust transport pathways from Lake Eyre, Australia
815 using Hysplit, *Atmos. Environ.*, 42, 6915–6925, 2008.

816 Meng, Z.Y., Xu, X.B., Yan, P., Ding, G.A., Tang, J., Lin, W.L., et al., 2009. Characteristics of trace
817 gaseous pollutants at a regional background station in Northern China. *Atmos.Chem. Phys.* 9,
818 927–936.

819 Ministry of Environmental Protection of China (MEP), Ambient air quality standards (GB 3095–
820 2012), 12 pp., China Environmental Science Press, Beijing, 2012.

821 Müller, T., Laborde, M., Kassell, G., and Wiedensohler, A.: Design and performance of a three-
822 wavelength LED-based total scatter and backscatter integrating nephelometer, *Atmos. Meas. Tech.*,
823 4, 1291–1303, doi:10.5194/amt-4-1291-2011, 2011.

824 Novelli, P.C., Masarile, K. A., Lang, P.M.: Distributions and recent changes of carbon monoxide
825 in the lower troposphere. *Journal of Geophysical Research Atmospheres*, 1998, 103(D15).

826 Pan, X.L., Kanaya, Y., Wang, Z.F., Liu, Y., Pochanart, P., Akimoto, H., Sun, Y.L., Dong, H.B., Li,
827 J., Irie, H., Takigawa, M., 2011. Correlation of black carbon aerosol and carbon monoxide in the
828 high-altitude environment of Mt. Huang in Eastern China. *Atmospheric Chemistry and Physics* 11,
829 9735-9747.

830 Petzold, A., Kopp, C., and Niessner, R.: The dependence of the specific attenuation cross-section on
831 black carbon mass fraction and particle size, *Atmos. Environ.*, 31, 661–672, 1997.

832 Qian, L., Yan, Y., and Qian, J.M.: An Observational Study on Physical and Optical Properties of
833 Atmospheric Aerosol in Autumn in Nanjing [J]. *Meteorological and Environmental Research* 2014,
834 5(2): 24 – 30

835 Roberts, P. T., Friedlander, S. K.: Analysis of sulfur in deposited aerosol particles by vaporization
836 and flame photometric detection. *Atmospheric Environment*, 1976, 10(5), 403-408.

837 Sassen, K., 2002. Indirect climate forcing over the western US from Asian dust storms. *Geophys..*
838 *Res. Lett.* 29.

839 Schleicher, N., Cen, K., Norra, S.: Daily variations of black carbon and element concentrations of
840 atmospheric particles in the Beijing megacity – Part 1: General temporal course and source

841 identification. *Chemie der Erde - Geochemistry*, 2013, 73(1):51-60.

842 Schmid, O., Artaxo, P., Arnott, W. P., Chand, D., Gatti, L. V., Frank, G. P., Hoffer, A., Schnaiter, M.,
843 and Andreae, M. O.: Spectral light absorption by ambient aerosols influenced by biomass burning
844 in the Amazon Basin. I: Comparison and field calibration of absorption measurement techniques,
845 *Atmos. Chem. Phys.*, 6, 3443–3462, doi:10.5194/acp-6-3443-2006, 2006.

846 Shao, M., Tang, X., Zhang, Y., Li, W., 2006. City clusters in China: air and surface water pollution.
847 *Front. Ecol. Environ.* 4, 353–361.

848 Shen, G. F., Yuan, S. Y., Xie, Y. N., Xia, S. J., Li, L., Yao, Y. K., Qiao, Y. Z., Zhang, J., Zhao, Q. Y.,
849 Ding, A. J.: Ambient levels and temporal variations of PM_{2.5} and PM₁₀ at a residential site in
850 the mega-city, Nanjing, in the western Yangtze River Delta, China. *J. Environ. Sci. Health Part A*
851 2014, 49, 171–178.

852 Shi, C., Wang, S., Liu, R., Zhou, R., Li, D., Wang, W., et al., 2015. A study of aerosol optical
853 properties during ozone pollution episodes in 2013 over Shanghai, China. *Atmos. Res.* 153, 235–
854 249.

855 Song, W.; Jia, H.; Huang, J.; Zhang, Y. A satellite-based geographically weighted regression model
856 for regional PM_{2.5} estimation over the Pearl River Delta region in China. *Remote Sens. Environ.*
857 2014, 154, 1–7.

858 Spackman, J. R., Schwarz, J. P., Gao, R. S., Watts, L. A., Thomson, D. S., Fahey, D. W., Holloway,
859 J. S., de Gouw, J. A., Trainer, M., and Ryerson, T. B.: Empirical correlations between black carbon
860 aerosol and carbon monoxide in the lower and middle troposphere, *Geophys. Res. Lett.*, 35(19),
861 L19816, doi:10.1029/2008GL035237, 2008.

862 Stein, A. F., Draxler, R. R., Rolph, G. D., Stunder, B. J. B., Cohen, M. D., and Ngan, F.: NOAA'S
863 Hysplit Atmospheric Transport and Dispersion Modeling System, *Bull. Amer. Meteor. Soc.*, 96,
864 2059–2077. doi: <http://dx.doi.org/10.1175/BAMS-D-14-00110.1>, 2016.

865 Streets, D.G., Gupta, S., Waldhoff, S.T., Wang, M.Q., Bond, T.C., Bo, Y.Y., 2001. Black carbon

866 emissions in China. *Atmospheric Environment* 35, 4281-4296.

867 Tegen, I., Schepanski, K.: The global distribution of mineral dust. *IOP Conference Series: Earth and*
868 *Environmental Science*, 2009, 7:012001.

869 Tu, J., Xia, Z. G., Wang, H. S., and Li, W. Q.: Temporal variations in surface ozone and its precursors
870 and meteorological effects at an urban site in China, *Atmos. Res.*, 85, 310–337, 2007.

871 van Donkelaar, A., Martin, R. V., Brauer, M., Kahn, R., Levy, R., Verduzco, C., and Villeneuve, P.
872 J.: Global estimates of ambient fine particulate matter concentrations from satellite-based aerosol
873 optical depth: development and application, *Environ. Health Perspectives*, 118, 847– 855, 2010.

874 Verma, R.L., Sahu, L.K., Kondo, Y., Takegawa, N., Han, S., Jung, J.S., Kin, Y.J., Fan, S., Sugimoto,
875 N., Shammaa, M.H., Zhang, Y.H., Zhao, Y., 2010. Temporal variations of black carbon in
876 Guangzhou, China, in summer 2006. *Atmospheric Chemistry and Physics* 10, 6471-6485.

877 von Schneidmesser, E., Monks, P. S., and Plass-Duelmer, C.: Global comparison of VOC and CO
878 observations in urban areas, *Atmos. Environ.*, 2010, 44(39): 5053–5064.

879 Wang, G. H., Huang, L. M., Gao, S. X., Gao, S. T., and Wang, L.S.: Characterization of watersoluble
880 species of PM₁₀ and PM_{2.5} aerosols in urban area in Nanjing, China, *Atmos. Environ.*, 36, 1299–
881 1307, 2002.

882 Wang, H. L., Zhuang, Y. H., Wang, Y., Sun, Y. L., Yuan, H., Zhuang, G. S., Hao, Z. P.: Long-term
883 monitoring and source apportionment of PM_{2.5}/PM₁₀ in Beijing, China. *Journal of*
884 *Environmental Sciences*, 2008, 20(11): 1323-1327.

885 Wang, M., Shao, M., Chen, W., Yuan, B., Lu, S., Zhang, Q., Zeng, L., Wang, Q.: A temporally and
886 spatially resolved validation of emission inventories by measurements of ambient volatile organic
887 compounds in Beijing, China. *Atmos. Chem. Phys.*, 2014, 14(12): 5871–5891.

888 Wang, P., Zhao, W.: Assessment of ambient volatile organic compounds (VOCs) near major roads
889 in urban Nanjing, China[J]. *Atmospheric Research*, 2008, 89(3):0-297.

890 Wang, M.Y., Cao, C.X., Li, G.S., and Singh, R.P.: Analysis of a severe prolonged regional haze

891 episode in the Yangtze River Delta, China, *Atmos. Environ.*, 102, 112-121, 2015.

892 Wang, T., Cheung, V.T.F., Anson, M., Li, Y.S., 2001a. Ozone and related gaseous pollutants in the
893 boundary layer of eastern China: overview of the recent measurements at a rural site. *Geophys.*
894 *Res. Lett.* 28, 2373–2376.

895 Wang, T., Cheung, T., Li, Y., Yu, X., Blake, D., 2002. Emission characteristics of CO, NO_x, SO₂
896 and indications of biomass burning observed at a rural site in eastern China. *J. Geophys. Res.-*
897 *Atmos.* 107.

898 Wang, T., Poon, C.N., Kwok, Y.H., Li, Y.S., 2003. Characterizing the temporal variability and
899 emission patterns of pollution plumes in the Pearl River Delta of China. *Atmos. Environ.* 37,
900 3539–3550.

901 Wang, T., Wong, C., Cheung, T., Blake, D., Arimoto, R., Baumann, K., et al., 2004. Relationships
902 of trace gases and aerosols and the emission characteristics at Lin'an, a rural site in eastern China,
903 during spring 2001. *J. Geophys. Res.-Atmos.* 109.

904 Wang, T., Xue, L. K., Brimblecombe, P., Lam, Y.F., Li, L., and Zhang, L.: Ozone pollution in China:
905 A review of concentrations, meteorological influences, chemical precursors, and effects. *Science*
906 *of the Total Environment.*, 575, 1582–1596, 2017.

907 Wang, T. J., Zhuang, B. L., Li, S., Liu, J., Xie, M., Yin, C. Q., Zhang, Y., Yuan, C., Zhu, J. L., Ji, L.
908 Q., and Han, Y.: The interactions between anthropogenic aerosols and the East Asian summer
909 monsoon using RegCCMS. *J. Geophys. Res. Atmos.*, 120, doi:10.1002/2014JD022877, 2015.

910 Wang, X., Li, J., Zhang, Y., Xie, S., Tang, X., 2009b. Ozone source attribution during a severe
911 photochemical smog episode in Beijing, China. *Sci. China, Ser. B: Chem.* 52, 1270–1280.

912 Wang, Y. Q., Stein, A. F., Draxler, R. R., de la Rosa, J. D., Zhang, X.Y.: Global sand and dust storms
913 in 2008: Observation and HYSPLIT model verification, *Atmos. Environ.*, 45, 6368-6381, 2011.

914 Wang, Y., Ying, Q., Hu, J., Zhang, H.: Spatial and temporal variations of six criteria air pollutants

915 in 31 provincial capital cities in China during 2013–2014. *Environment International*, 2014,
916 73:413–422.

917 Wang, Y., Wang, X., Kondo, Y., Kajino, M., Munger, J.W., Hao, J., 2011b. Black carbon and its
918 correlation with trace gases at a rural site in Beijing: top-down constraints from ambient
919 measurements on bottom-up emissions. *Journal of Geophysical Research* 116, D24304.

920 Wang, Y., Zhuang, G. S., Zhang, X. Y., Huang, K., Xu, Chang, Tang, A. H., Chen, J. M., and An, Z.
921 S.: The ion chemistry, seasonal cycle, and sources of PM_{2.5} and TSP aerosol in Shanghai, *Atmos.*
922 *Environ.*, 40, 2935–2952, 2006.

923 Wang, Z., Li, J., Wang, X., Pochanart, P., Akimoto, H.: Modeling of Regional High Ozone Episode
924 Observed at Two Mountain Sites (Mt. Tai and Huang) in East China[J]. *Journal of Atmospheric*
925 *Chemistry*, 2006, 55(3):253-272.

926 Wang, Z., Li, Y., Chen, T., Zhang, D., Sun, F., Pan, L.: Spatial-temporal characteristics of PM_{2.5} in
927 Beijing in 2013. *Acta Geogr. Sin.* 2015, 70, 110–120.

928 Weingartner, E., Saathoff, H., Schnaiter, M., Streit, N., Bitnar, B., and Baltensperger, U.: Absorption
929 of light by soot particles: determination of the absorption coefficient by means of aethalometers,
930 *J. Aerosol Sci.*, 34, 1445–1463, doi:10.1016/S0021- 8502(03)00359-8, 2003.

931 Wu, D., Liu, Q., Lian, Y., Bi, X., Li, F., Tan, H., Liao, B., Chen, H., Hazy weather formation and
932 visibility deterioration resulted from fine particulate (PM_{2.5}) pollutions in Guangdong and
933 Hong Kong. *J. Environ. Sci. Circumst.* 2012, 32, 2660–2669.

934 Wu, Y.; Guo, J.; Zhang, X.; Tian, X.; Zhang, J.; Wang, Y.; Duan, J.; Li, X. Synergy of satellite and
935 ground based observations in estimation of particulate matter in eastern China. *Sci. Total Environ.*
936 2012, 433, 20–30.

937 Xiao, Z., Bi, X., Feng, Y., Wang, Y., Zhou, J., Fu, X., Weng, Y., 2012. Source apportionment of
938 ambient PM₁₀ and PM_{2.5} in urban area of Ningbo City. *Res. Environ. Sci. (China)* 5, 549–555.

939 Xiao, Z. M., Zhang, Y. F., Hong, S. M., Bi, X. H., Jiao, L., Feng, Y. C., Wang, Y. Q.: Estimation of
940 the Main Factors Influencing Haze, Based on a Long-term Monitoring Campaign in Hangzhou,
941 China. *Aerosol & Air Quality Research.*, 2011, 11, 873-882.

942 Xie, M., Zhu, K.G., Wang, T.J., Chen, P.L., Han, Y., Li, S., Zhuang, B.L., and Shu, L., Temporal
943 characterization and regional contribution to O₃ and NO_x at an urban and a suburban site in
944 Nanjing, China. *Science of the Total Environment.*, 551–552, 533–545, 2016

945 Xue, L., Wang, T., Louie, P.K.K., Luk, C.W.Y., Blake, D.R., Xu, Z., 2014a. Increasing external
946 effects negate local efforts to control ozone air pollution: a case study of Hong Kong and
947 implications for other Chinese cities. *Environ. Sci. Technol.* 48, 10769–10775.

948 Yang, S. J., He, H. P, Lu, S. L., Chen, D., Zhu, J. X.: Quantification of crop residue burning in the
949 field and its influence on ambient air quality in Suqian, China. *Atmospheric Environment*,
950 2008,42(9):1961-1969.

951 Yan, S.; Cao, H.; Chen, Y.; Wu, C.; Hong, T.; Fan, H. Spatial and temporal characteristics of air
952 quality and air pollutants in 2013 in Beijing. *Environ. Sci. Pollut. Res.* 2016, 23, 1–12.

953 Yin, S., Wang, X.F, Xiao, Y., Tani, H., Zhong, G.S., Sun, Z.Y.: Study on spatial distribution of crop
954 residue burning and PM_{2.5} change in China. *Environmental Pollution*, 2016, 220(Pt A):204-221.

955 Yi, R., Wang, Y.L., Zhang, Y.J., Shi, Y., Li, M.S., 2015. Pollution characteristics and influence
956 factors of ozone in Yangtze River Delta. *Acta Sci. Circumst.* 35, 2370–2377 (in Chinese).

957 Yu, J., Wang, W., Zhou, J., Xu, D., Zhao, Q., He, L., 2015. Analysis of pollution characteristics and
958 sources of PM_{2.5} in winter of Ningbo City. *Environ. Sci. Technol. (China)* 8, 150–155.

959 Zhang, Q., Streets, D.G., Carmichael, G.R., He, K.B., Huo, H., Kannari, A., Klimont, Z., Park, I.S.,
960 Reddy, S., Fu, J.S., Chen, D., Duan, L., Lei, Y., Wang, L.T., Yao, Z.L., 2009. Asian emissions in
961 2006 for the NASA INTEX-B mission. *Atmos. Chem. Phys.* 9, 5131–5153.

962 Zhang, Y. H., Hu, M., Zhong, L. J., Wiedensohler, A., Liu, S. C., Andreae, M. O., Wang, W., Fan, S.
963 J.: Regional integrated experiments on air quality over Pearl River Delta 2004 (PRIDE-PRD2004):

964 overview. *Atmos. Environ.* 42, 6157–6173, 2008.

965 Zhang, X. Y., Wang, Y. Q., Niu, T., Zhang, X. C., Gong, S.L., Zhang, Y.M., Sun, T.Y., 2012.

966 Atmospheric aerosol compositions in China: spatial/temporal variability, chemical signature,

967 regional haze distribution and comparisons with global aerosols. *Atmospheric Chemistry and*

968 *Physics* 12, 779-799.

969 Zhang, X.Y., Wang, Y.Q., Zhang, X.C., Guo, W., Gong, S.L., 2008. Carbonaceous aerosol

970 composition over various regions of China during 2006. *Journal of Geophysical Research* 113,

971 D14111.

972 Zhang, Y. L., Cao, F. Fine particulate matter (PM_{2.5}) in China at a city level. *Sci. Rep.* 2015, 5,

973 14884.

974 Zhang, Y., Shao, K., Tang, X., 1998. The study of urban photochemical smog pollution in China.

975 *Acta Scientiarum Naturalium-Universitatis Pekinensis* 34, 392–400.

976 Zheng, J., Zhong, L., Wang, T., Louie, P.K.K., Li, Z., 2010. Ground-level ozone in the Pearl River

977 Delta region: analysis of data from a recently established regional air quality monitoring network.

978 *Atmos. Environ.* 44, 814–823.

979 Zhu, J. L., Wang, T. J., Talbot, R. H., Mao, H. T., Hall, C. B., Yang, X. Q., Fu, C. B., Zhuang, B. L.,

980 Li, S., Han, Y., Huang, X., 2012. Characteristics of atmospheric Total Gaseous Mercury (TGM)

981 observed in urban Nanjing, China. *Atmospheric Chemistry and Physics* 12, 12103-12118.

982 Zhuang, B.L., Liu, L., Shen, F.H., Wang, T.J., Han, Y., 2010. Semidirect radiative forcing of internal

983 mixed black carbon cloud droplet and its regional climatic effect over China. *Journal of*

984 *Geophysical Research* 115, D00K19.

985 Zhuang, B. L., Liu, Q., Wang, T. J., Yin, C. Q., Li, S., Xie, M., Jiang, F., Mao, H.T., 2013.

986 Investigation on semi-direct and indirect climate effects of fossil fuel black carbon aerosol over

987 China. *Theoretical and Applied Climatology* 114, 651-672.

988 Zhuang, B. L., Li, S., Wang, T. J., Deng, J. J., Xie, M., Yin, C. Q., and Zhu, J. L.: Direct radiative
989 forcing and climate effects of anthropogenic aerosols with different mixing states over China,
990 *Atmos. Environ.*, 79, 349–361, doi:10.1016/j.atmosenv.2013.07.004, 2013b.

991 Zhuang, B. L., Li, S., Wang, T. J., Liu, J., Chen, H. M., Chen, P. L., Li, M. M., Xie, M.: Interaction
992 between the Black Carbon Aerosol Warming Effect and East Asian Monsoon Using RegCM4.
993 *Journal of Climate*, 2018, 31(22):9367-9388.

994 Zhuang, B. L., Wang, T. J., Liu, J., Li, S., Xie, M., Han, Y., Chen, P. L., Hu, Q. D., Yang X.Q., Fu,
995 C. B., and Zhu, J. L.: The surface aerosol optical properties in the urban area of Nanjing, west GTH
996 River Delta, China. *Atmos. Chem. Phys.*, 17, 1143–1160, doi:10.5194/acp-17-1143-2017, 2017.

997 Zhuang, B. L., Wang, T. J., Liu, J., Li, S., Xie, M., Yang, X. Q., Fu, C. B., Sun, J. N., Yin, C. Q.,
998 Liao, J. B., Zhu, J. L., and Zhang, Y.: Continuous measurement of black carbon aerosol in urban
999 Nanjing of Yangtze River Delta, China, *Atmos. Environ.*, 89, 415–424, 2014b.

1000 Zhuang, B. L., Wang, T. J., Liu, J., Ma, Y., Yin, C. Q., Li, S., Xie, M., Han, Y., Zhu, J. L., Yang, X.
1001 Q., and Fu, C. B.: Absorption coefficient of urban aerosol in Nanjing, west Yangtze River Delta,
1002 China, *Atmos. Chem. Phys.*, 15, 13633–13646, doi:10.5194/acp-15-13633-2015, 2015.

1003 Zhuang, B. L., Wang, T. J., Li, S., Liu, J., Talbot, R., Mao, H. T., Yang, X. Q., Fu, C. B., Yin, C. Q.,
1004 Zhu, J. L., Che, H. Z., and Zhang, X. Y.: Optical properties and radiative forcing of urban aerosols
1005 in Nanjing, China, *Atmos. Environ.*, 83, 43–52, 2014a.

1006
1007
1008
1009
1010
1011

1012 **Figure and Table Caption**

1013 Fig 1. Time series of (a) concentrations and (b) optical properties of PM₁₀, PM_{2.5}, and BC at Gulou
1014 site from September 2016 to February 2017.

1015

1016 Fig 2. Seasonal variations of (a) BC, (b) PM_{2.5}, and (c) PM₁₀. The 10, 25, 50, 75, and 90% percentile
1017 values of each are shown in black, and red markers represent the monthly averages.

1018

1019 Fig 3. 6-month mean diurnal variations of BC, PM_{2.5}, and PM₁₀ at Gulou site from September 2016
1020 to February 2017.

1021

1022 Fig.4 Time series of O₃, NO_y, NO_x, and CO concentrations at Gulou site from September 2016 to
1023 February 2017.

1024

1025 Fig 5. Seasonal variations of (a) O₃, (b) NO_x, (c) CO, and (d) NO_y. The 10, 25, 50, 75, and 90%
1026 percentile values of each are shown in black, and red markers represent the monthly averages.

1027

1028 Fig 6. 6-month mean diurnal variations of (a) trace gases and (b) UV at Gulou site from September
1029 2016 to February 2017.

1030

1031 Fig 7. Scatter plots of (a) O₃-NO_x color-coded with air temperature (T) and (b) PM_{2.5}-Vis color-
1032 coded with relative humidity (RH).

1033

1034 Fig 8. Scatter plots of (a) PM_{2.5}-O₃ and (b) BC-O₃ color-coded with air temperature (T).

1035

1036 Fig 9. Scatter plots of (a) O₃-UV and (b) PM_{2.5}-UV color coded with O₃.

1037

1038 Fig 10. Scatter plots of (a) CO-NO_x, (b) PM_{2.5}-NO_x, and (c) BC-NO_x color-coded with O₃.

1039

1040 Fig 11. Clusters of 96 h back trajectories arriving at Gulou site at 100 m in 2016 fall.

1041

1042 Fig 12. The 10, 25, 50, 75, and 90% percentile values in each cluster of back trajectories in 2016

1043 fall of (a) BC, (b) PM_{2.5}, (c) PM_{2.5}/PM₁₀, (d) CO, (e) O₃, (f) NO_y, (g) α_{ts} , and (h) ω_0 . Black
1044 markers represent the averages.

1045

1046 Fig 13. Clusters of 96 h back trajectories arriving at Gulou site at 100m in 2016 winter.

1047

1048 Fig 14. The 10, 25, 50, 75, and 90% percentile values in each cluster of back trajectories in 2016

1049 winter of (a) BC, (b) PM_{2.5}, (c) PM_{2.5}/PM₁₀, (d) CO, (e) O₃, (f) NO_y, (g) α_{ts} , and (h) ω_0 . Black
1050 markers represent the averages.

1051

1052 Fig 15. Time series during December 3-6, 2016, for (a) PM_{2.5}, BC and O₃ with associated
 1053 metrological parameters, trace gases and (b) optical parameters. Red markers represent O₃ over
 1054 daily maximum average during winter. Weather charts on (c) 4th and (d) 5th December. (e) 96h
 1055 backward trajectories analysis ending at 1200 UTC on 5th December.

1056

1057 Table 1 Measurements at Gulou site.

1058

1059 Table 2 Statistics of general meteorological parameters at Gulou site during the study period.

1060

1061 Table 3 Statistics of the three particles at Gulou site during the study period.

1062

1063 Table 4 Statistics of trace gases during the study period.

1064

1065 Table 5 Statistics of maximum and number of exceedances of O₃ and PM_{2.5} compared with the
 1066 National Ambient Air Quality Standards in China.

1067

1068 Table 6 Statistics of aerosols with and without rainfall at Gulou site during the study period.

1069 **Table**

1070 Table 1 Measurements at Gulou site.

Measurement		Instrument	Resolution
Meteorological parameters	T (°C)	Thermo Instruments, THOM 1405-DF	
	P (atm)	Thermo Instruments, THOM 1405-DF	
	RH (%)	Thermo Instruments, THOM 1405-DF	
	Rainfall (mm)		
	Vis (m)	Visibility Meter, GSN-1	
	UV (W/m ²)		
Particles	BC (ng/m ³)	Aethalometer, Model AE-31	1 ng/m ³
	PM _{2.5} (µg/m ³)	Thermo Instruments, THOM 1405-DF	0.1µg/m ³
	PM ₁₀ (µg/m ³)	Thermo Instruments, THOM 1405-DF	0.1µg/m ³
Gaseous pollutant	CO (ppb)	Thermo Instruments, TEI 48i	1 ppb
	NO _x (ppb)	Thermo Instruments, TEI 42i	0.4 ppb
	NO _y (ppb)	Thermo Instruments, TEI 42iY	0.4 ppb
	O ₃ (ppb)	Thermo Instruments, TEI 49i	0.01 ppb
Optical parameters	SC (Mm ⁻¹)	Nephelometer, Aurora 3000	10 ⁻³ Mm ⁻¹
	BSP (Mm ⁻¹)	Nephelometer, Aurora 3000	10 ⁻³ Mm ⁻¹
	AAC (Mm ⁻¹)	Aethalometer, Model AE-31	10 ⁻³ Mm ⁻¹

1071

1072 Table 2 Statistics of general meteorological parameters at Gulou site during the study period.

Month	Temp (°C)	Pres (hPa)	RH (%)	Rainfall (mm)	Vis (km)	UV (W/m ²)
Sep	24.88	996.97	69.41	2.34	11.84	10.36
Oct	18.37	1003.01	85.01	3.12	9.07	5.28
Nov	12.36	1007.87	77.15	1.19	8.99	5.67
Dec	8.74	1010.53	70.33	0.81	7.61	5.03
Jan	6.49	1010.89	70.65	0.59	9.23	4.94
Feb	7.72	1009.65	59.99	0.45	10.24	7.04

1073

1074

1075

Table 3 Statistics of particles at Gulou site during the study period.

	SON	DJF	Cold seasons		
	Mean ± STD	Mean ± STD	Mean ± STD	Maximum	Minimum
BC (µg/m ³)	2.126 ± 1.457	3.083 ± 1.827	2.602 ± 1.720	15.609	0.064
PM _{2.5} (µg/m ³)	43.1 ± 25.4	73.2 ± 40.0	58.2 ± 36.8	256.2	0.8
PM ₁₀ (µg/m ³)	67.6 ± 39.1	105.0 ± 54.0	86.3 ± 50.8	343.4	1.1

1076

1077

1078

Table 4 Statistics of trace gases at Gulou site during the study period.

	SON	DJF	Cold seasons		
	Mean ± STD	Mean ± STD	Mean ± STD	Maximum	Minimum
CO (ppb)	753 ± 353	950 ± 388	851 ± 384	2852	176
NO _x (ppb)	21.4 ± 13.4	25.6 ± 15.5	23.5 ± 14.7	80.0	2.7
NO _y (ppb)	28.6 ± 20.5	37.0 ± 23.1	32.8 ± 22.3	158.4	3.6
O ₃ (ppb)	42.3 ± 40.1	33.1 ± 24.4	37.7 ± 35.5	235.7	0.2

1079

1080

1081

1082

1083

1084

1085

1086

1087

1088

1089

1090

1091

Table 5 Statistics of maximum and number of exceedances of O₃ and PM_{2.5} compared with the

1092

National Ambient Air Quality Standards in China.

Aerosol	Mean \pm STD ($\mu\text{g}/\text{m}^3$)	Max ($\mu\text{g}/\text{m}^3$)	N.o.E.
PM _{2.5}	58.2 \pm 36.8	256.2	48
PM ₁₀	86.3 \pm 50.8	343.4	14
O ₃	80.8 \pm 71.8	235.7	37

1093 N.o.E. of PM_{2.5} accounts for days with 24 h average over 75 $\mu\text{g}/\text{m}^3$. N.o.E. of PM₁₀ accounts for days
1094 with 24 h average over 150 $\mu\text{g}/\text{m}^3$. N.o.E of O₃ accounts for days with maximum 8 h average exceed
1095 160 $\mu\text{g}/\text{m}^3$.

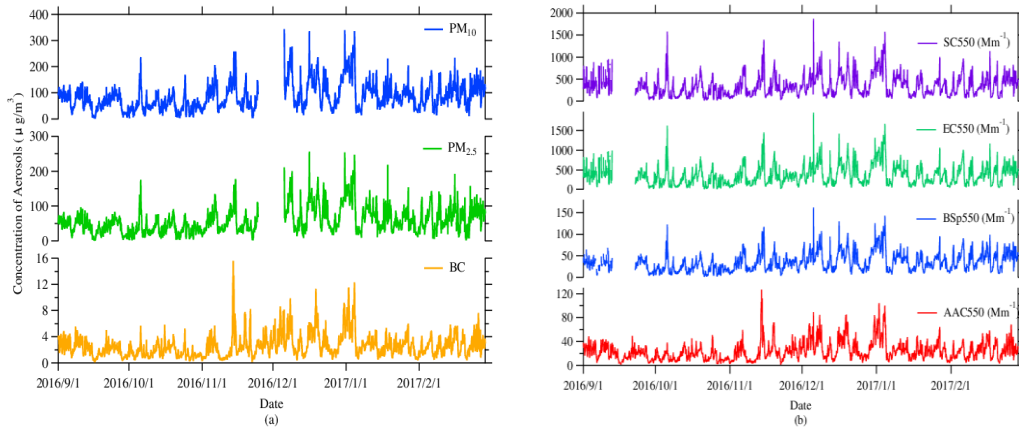
1096
1097

1098 Table 6 Statistics of aerosols with and without rainfall at Gulou site during the study period.

Aerosols	With Rainfall			Without Rainfall		
	Mean \pm STD	Maximum	Minimum	Mean \pm STD	Maximum	Minimum
BC ($\mu\text{g}/\text{m}^3$)	1.676 \pm 1.261	8.256	0.064	2.723 \pm 1.735	15.608	0.211
PM _{2.5} ($\mu\text{g}/\text{m}^3$)	31.2 \pm 27.6	218.4	1.2	61.9 \pm 36.3	256.2	0.8
PM ₁₀ ($\mu\text{g}/\text{m}^3$)	54.3 \pm 44.8	307.3	3.9	89.1 \pm 47.3	319.6	4.5
CO (ppb)	659 \pm 240	2194	176	876 \pm 392	2852	228
NO _x (ppb)	20.4 \pm 12.7	75.5	2.9	23.9 \pm 14.9	80	2.7
NO _y (ppb)	25.2 \pm 16.8	110.3	3.6	33.8 \pm 22.8	158.4	5.2
O ₃ (ppb)	22.3 \pm 17.1	81.7	0.3	39.7 \pm 34.6	235.7	0.2

1099
1100
1101
1102
1103
1104
1105
1106
1107
1108
1109
1110
1111
1112

1113 **Figure**



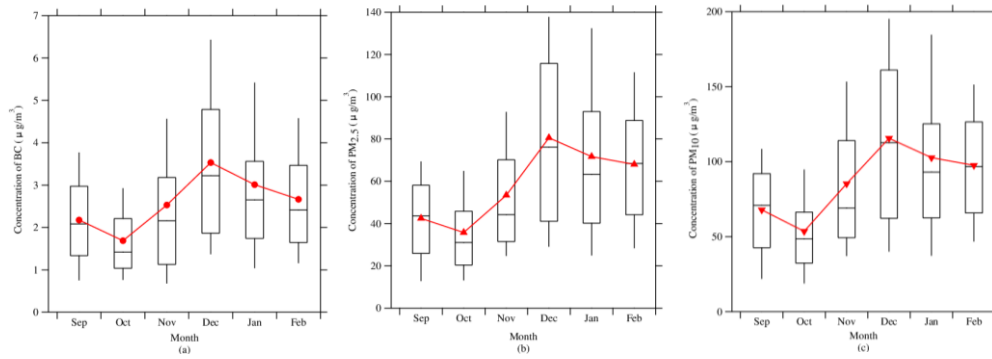
1114

1115 Fig 1. Time series of (a) concentrations and (b) optical properties of PM_{10} , $\text{PM}_{2.5}$, and BC at Gulou

1116

site from September 2016 to February 2017.

1117

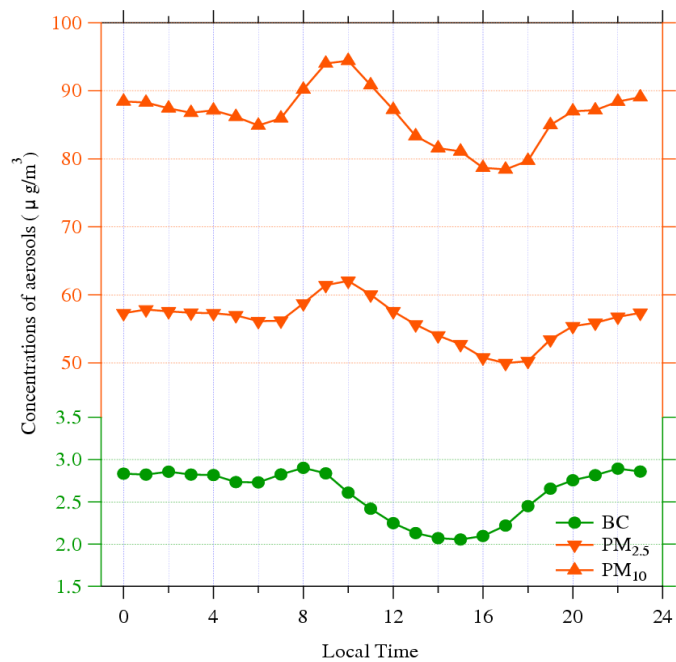


1118

1119 Fig 2. Seasonal variations of (a) BC, (b) $\text{PM}_{2.5}$, and (c) PM_{10} . The 10, 25, 50, 75, and 90%

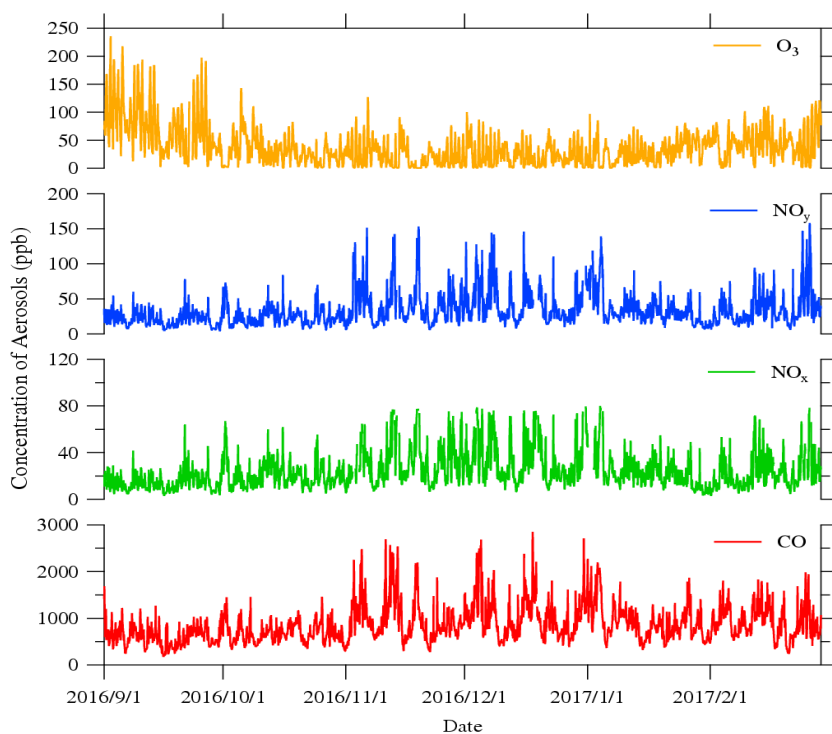
1120

percentile values of each are shown in black, and red markers represent the monthly averages.



1121
 1122
 1123
 1124
 1125

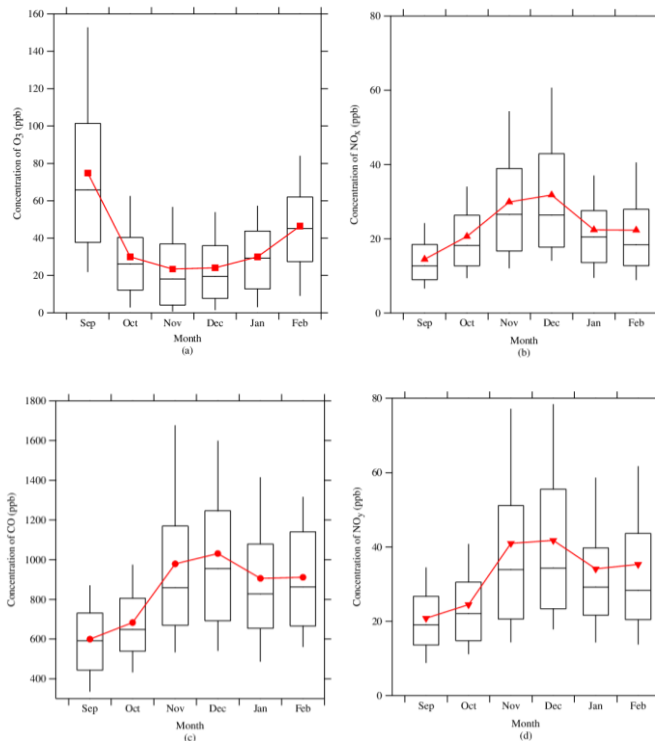
Fig 3. 6-month mean diurnal variations of BC, PM_{2.5}, and PM₁₀ at Gulou site from September 2016 to February 2017.



1126
 1127
 1128
 1129
 1130

Fig.4 Time series of O₃, NO_y, NO_x, and CO concentrations at Gulou site from September 2016 to February 2017.

1131



1132

1133

Fig 5. Seasonal variations of (a) O₃, (b) NO_x, (c) CO, and (d) NO_y. The 10, 25, 50, 75, and

1134

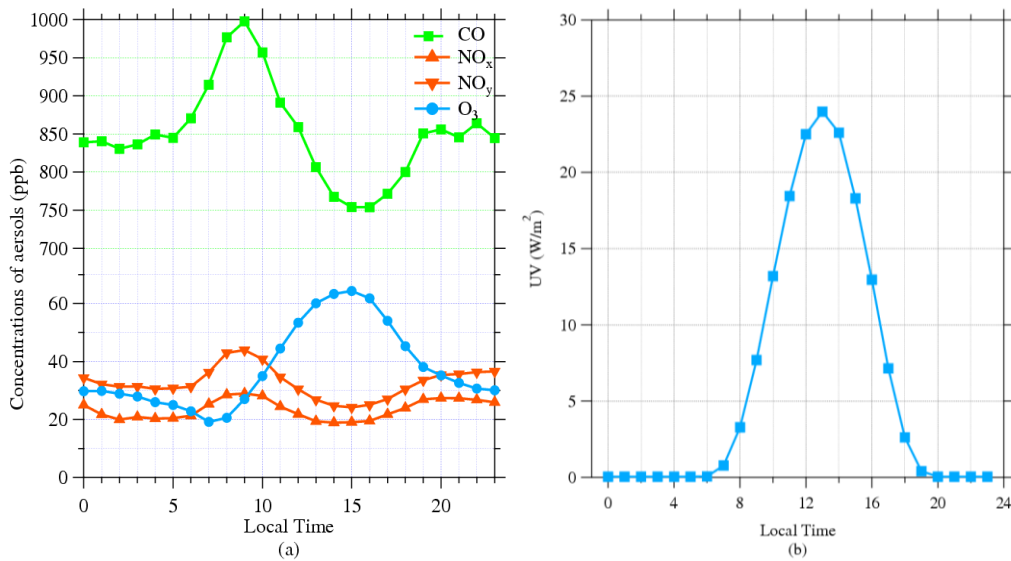
90% percentile values of each are shown in black, and red markers represent the monthly

1135

averages.

1136

1137



1138

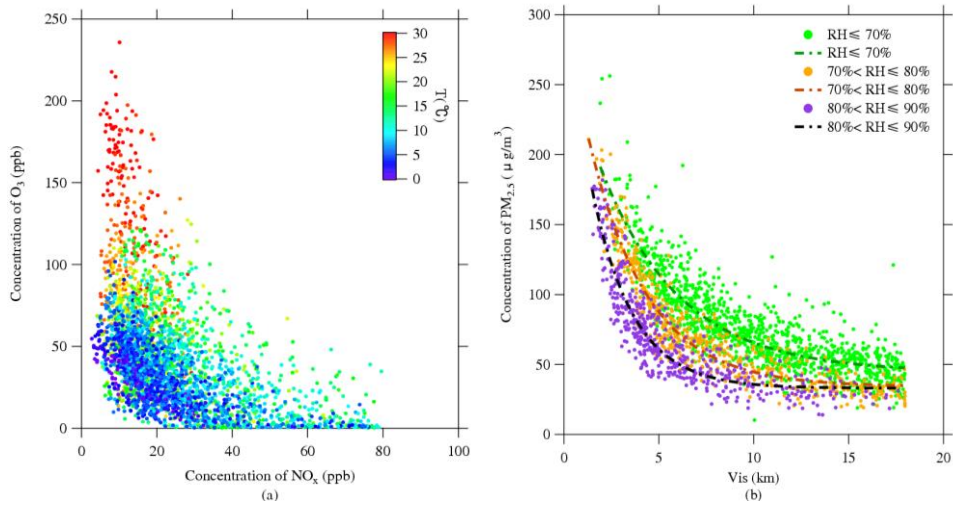
1139

Fig 6. 6-month mean diurnal variations of (a) trace gases and (b) UV at Gulou site from

1140

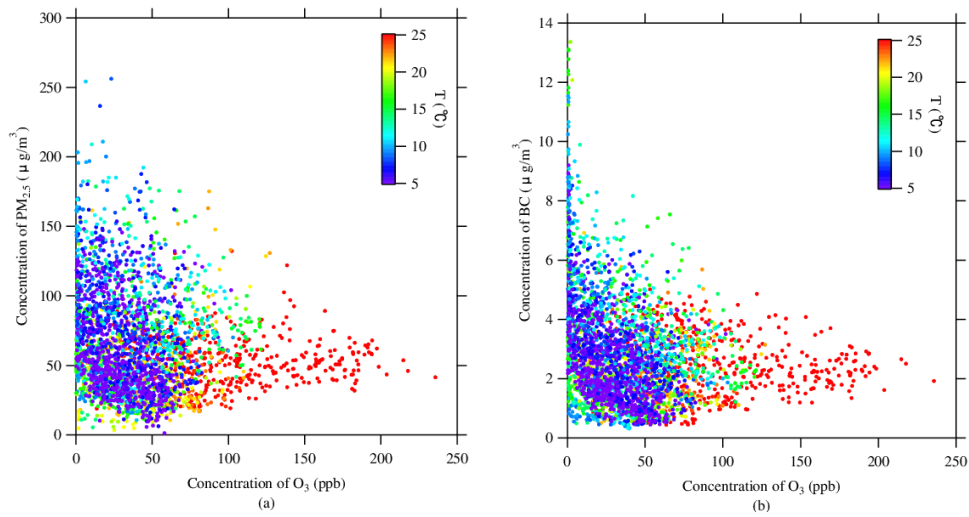
September 2016 to February 2017.

1141
1142



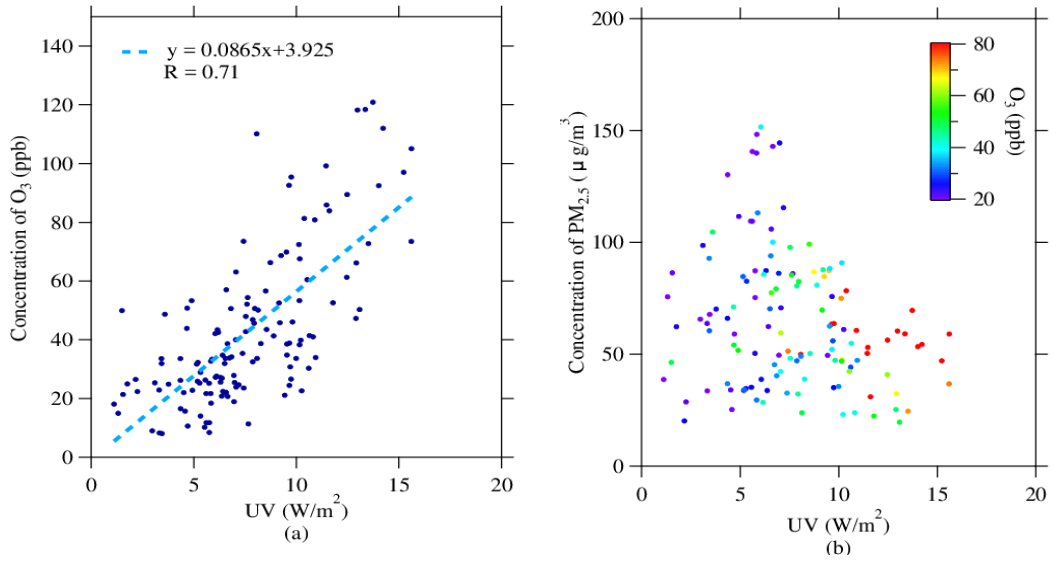
1143
1144
1145
1146
1147

Fig 7. Scatter plots of (a) O_3 - NO_x color-coded with air temperature (T) and (b) $PM_{2.5}$ -Vis color-coded with relative humidity (RH).



1148
1149

Fig 8. Scatter plots of (a) $PM_{2.5}$ - O_3 and (b) BC- O_3 color-coded with air temperature (T).



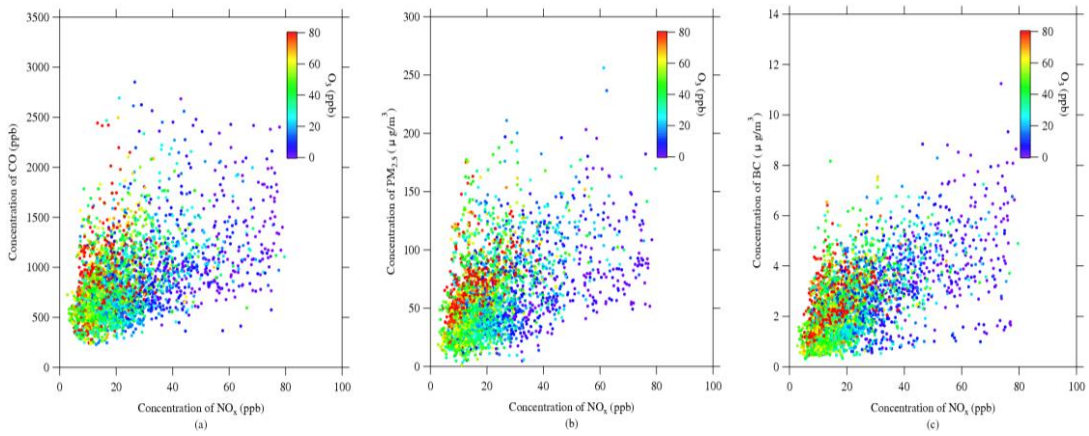
1150

1151

Fig 9. Scatter plots of (a) O_3 -UV and (b) $PM_{2.5}$ -UV color coded with O_3 .

1152

1153



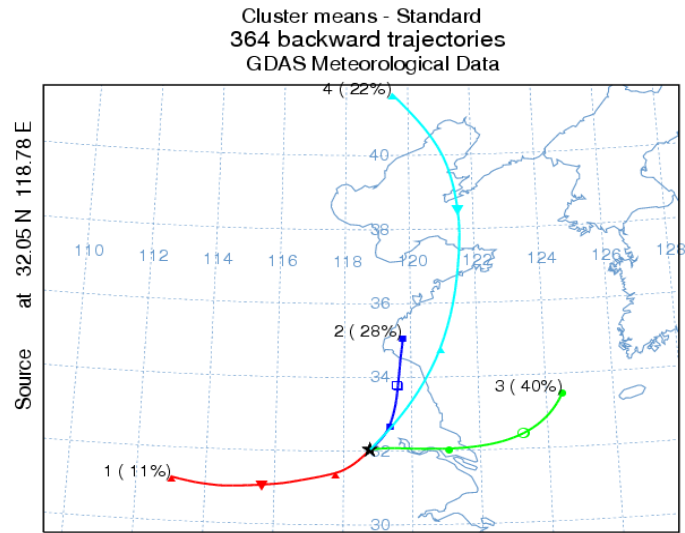
1154

1155

Fig 10. Scatter plots of (a) CO- NO_x , (b) $PM_{2.5}$ - NO_x , and (c) BC- NO_x color-coded with O_3 .

1156

1157



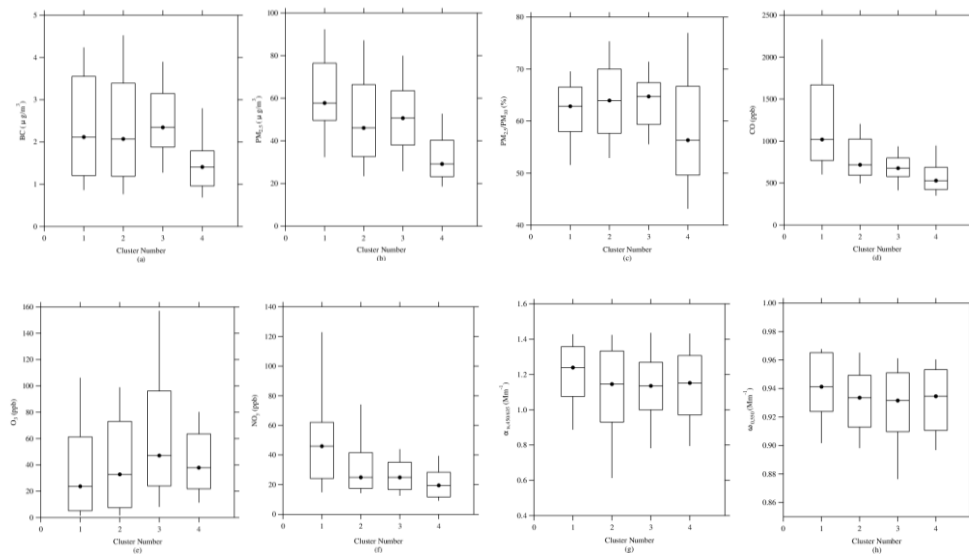
1158

1159

Fig 11. Clusters of 96 h back trajectories arriving at Gulou site at 100 m in 2016 fall.

1160

1161



1162

1163

1164

Fig 12. The 10, 25, 50, 75, and 90% percentile values in each cluster of back trajectories in 2016

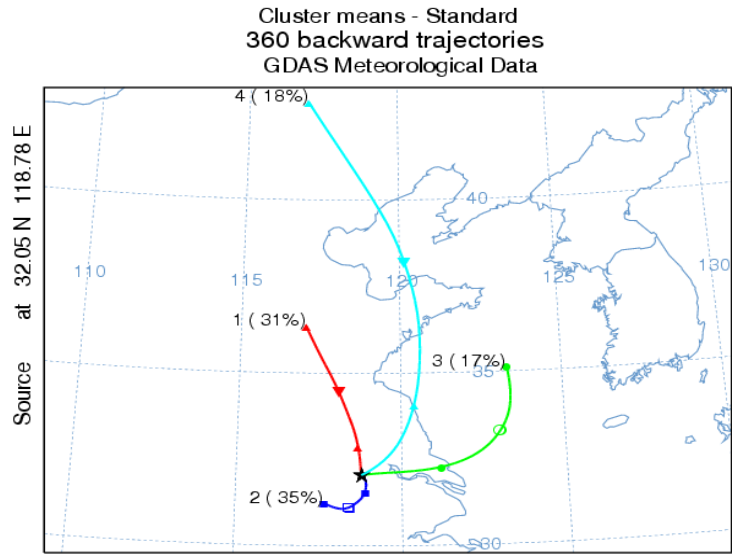
1165

fall of (a) BC, (b) PM_{2.5}, (c) PM_{2.5}/PM₁₀, (d) CO, (e) O₃, (f) NO_y, (g) α_{ts} , and (h) ω_0 . Black

1166

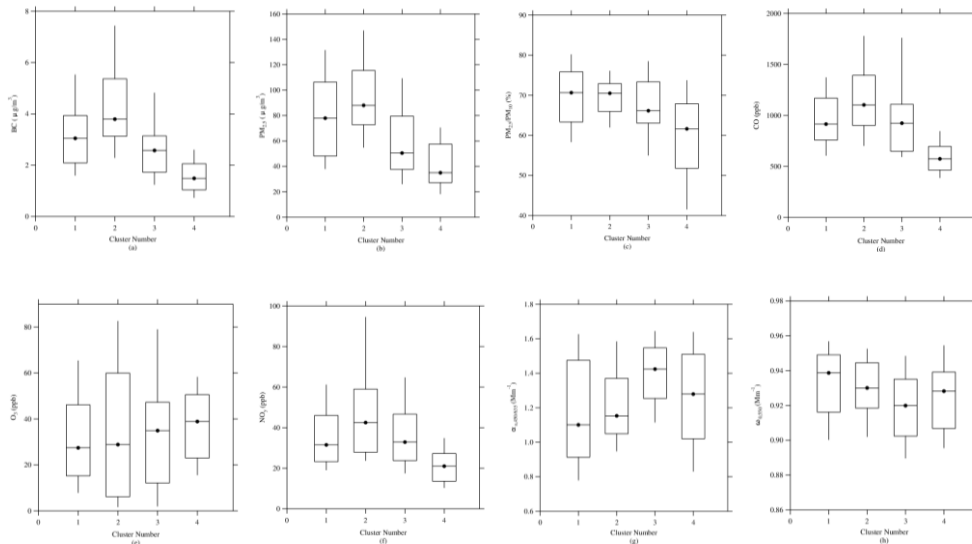
markers represent the averages.

1167



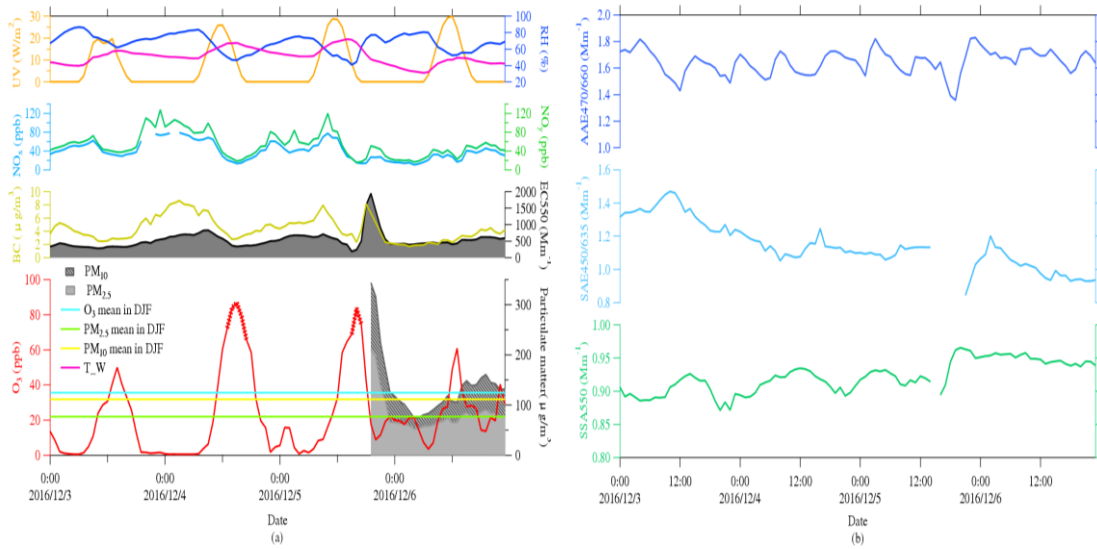
1168
1169
1170
1171

Fig 13. Clusters of 96 h back trajectories arriving at Gulou site at 100m in 2016 winter.

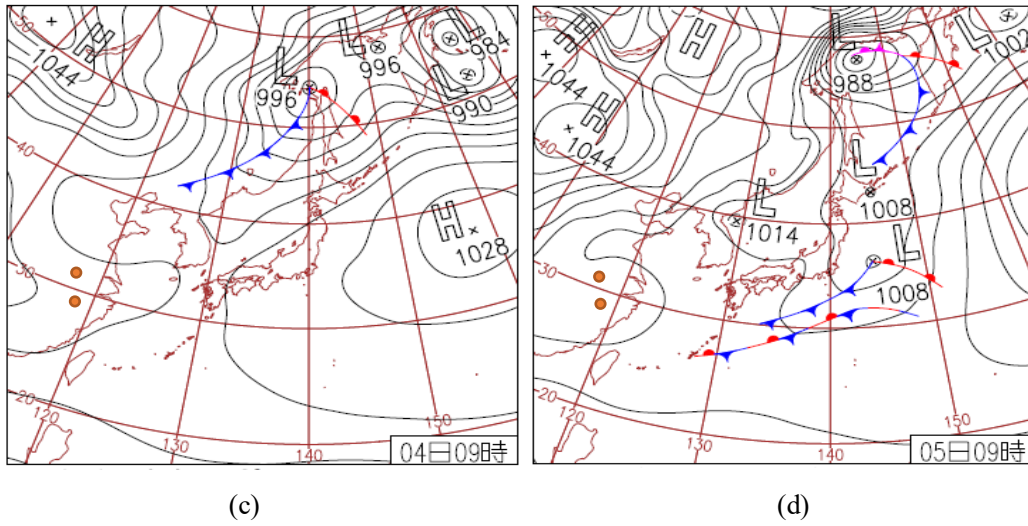


1172
1173
1174
1175
1176
1177
1178

Fig 14. The 10, 25, 50, 75, and 90% percentile values in each cluster of back trajectories in 2016 winter of (a) BC, (b) PM_{2.5}, (c) PM_{2.5}/PM₁₀, (d) CO, (e) O₃, (f) NO_y, (g) α_{ts} , and (h) ω_0 . Black markers represent the averages.

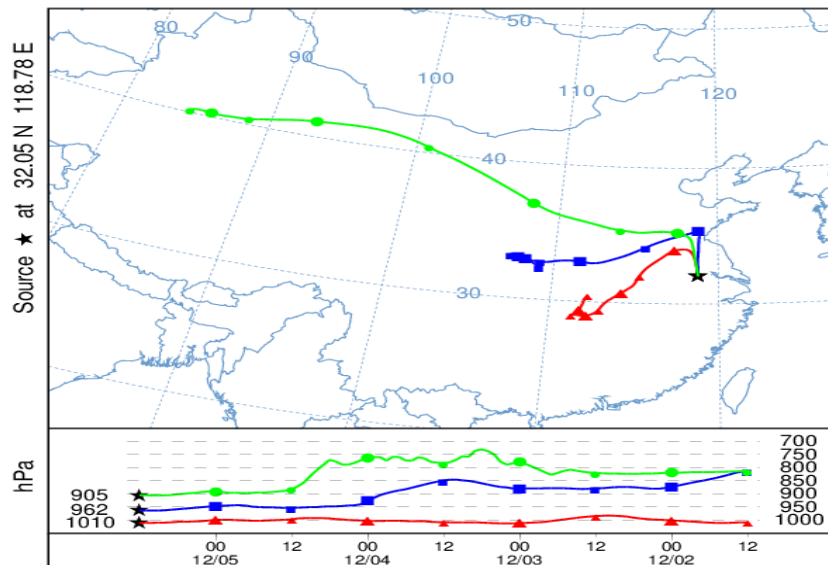


1179



1180
1181

NOAA HYSPLIT MODEL
Backward trajectories ending at 1200 UTC 05 Dec 16
GDAS Meteorological Data



1182
1183

(e)

1184 Fig 15. Time series during December 3-6, 2016, for (a) PM_{2.5}, BC and O₃ with associated
1185 meteorological parameters, trace gases and (b) optical parameters. Red markers represent O₃ over
1186 daily maximum average during winter. Weather charts on (c) 4th and (d) 5th December. (e) 96h
1187 backward trajectories analysis ending at 1200 UTC on 5th December.